of the
ROYAL ASTRONOMICAL SOCIETY

MNRAS 486, 453–461 (2019) Advance Access publication 2019 March 29 doi:10.1093/mnras/stz913



The newborn planet population emerging from ring-like structures in discs

Giuseppe Lodato , ¹* Giovanni Dipierro , ² Enrico Ragusa , ^{1,2} Feng Long, ³ Gregory J. Herczeg, ³ Ilaria Pascucci, ^{4,5} Paola Pinilla, ⁶ Carlo F. Manara, ⁷ Marco Tazzari , ⁸ Yao Liu, ^{9,10} Gijs D. Mulders, ^{5,11} Daniel Harsono, ¹² Yann Boehler, ¹³ François Ménard, ¹³ Doug Johnstone, ^{14,15} Colette Salyk, ¹⁶ Gerrit van der Plas, ¹³ Sylvie Cabrit, ¹⁷ Suzan Edwards, ¹⁸ William J. Fischer, ¹⁹ Nathan Hendler, ⁴ Brunella Nisini, ²⁰ Elisabetta Rigliaco, ²¹ Henning Avenhaus, ⁹ Andrea Banzatti and Michael Gully-Santiago²²

Affiliations are listed at the end of the paper

Accepted 2019 March 25. Received 2019 March 12; in original form 2018 November 23

ABSTRACT

ALMA has observed a plethora of ring-like structures in planet-forming discs at distances of 10-100 au from their host star. Although several mechanisms have been invoked to explain the origin of such rings, a common explanation is that they trace new-born planets. Under the planetary hypothesis, a natural question is how to reconcile the apparently high frequency of gap-carving planets at 10-100 au with the paucity of Jupiter-mass planets observed around main-sequence stars at those separations. Here, we provide an analysis of the new-born planet population emerging from observations of gaps in discs, under the assumption that the observed gaps are due to planets. We use a simple estimate of the planet mass based on the gap morphology, and apply it to a sample of gaps recently obtained by us in a survey of Taurus with ALMA. We also include additional data from recent published surveys, thus analysing the largest gap sample to date, for a total of 48 gaps. The properties of the purported planets occupy a distinctively different region of parameter space with respect to the known exo-planet population, currently not accessible through planet finding methods. Thus, no discrepancy in the mass and radius distribution of the two populations can be claimed at this stage. We show that the mass of the inferred planets conforms to the theoretically expected trend for the minimum planet mass needed to carve a dust gap. Finally, we estimate the separation and mass of the putative planets after accounting for migration and accretion, for a range of evolutionary times, finding a good match with the distribution of cold Jupiters.

Key words: accretion, accretion discs-planets and satellites: formation-protoplanetary discs.

1 INTRODUCTION

The discovery of the HL Tau disc and its system of rings (ALMA Partnership et al. 2015) has marked a new era in our understanding of the gas and dust discs around young stellar objects. Disc substructures appear to be commonplace, and in particular, the most frequently observed structures are regular, almost axisymmetric rings (Andrews et al. 2016; Isella et al. 2016; Fedele et al. 2017, 2018; Clarke et al. 2018; Dipierro et al. 2018; Hendler et al. 2018;

van Terwisga et al. 2018; Liu et al. 2019). Many theoretical models have been proposed to explain the origin of such rings, including dead zones (Ruge et al. 2016), condensation fronts (Zhang, Blake & Bergin 2015), self-induced dust pile-ups (Gonzalez et al. 2015), self-induced reconnection in magnetized disc-wind systems (Suriano et al. 2018) or large-scale vortices (Barge et al. 2017). However, another natural explanation is to associate the gap in the disc to the presence of an embedded planet (Huang et al. 2018; Long et al. 2018). This hypothesis has been tested extensively by comparing the disc emission obtained from ALMA observations to that computed from detailed hydrodynamical and radiative transfer simulations (e.g. Dipierro et al. 2015; Clarke et al. 2018).

* E-mail: giuseppe.lodato@unimi.it

© 2019 The Author(s)
Published by Oxford University Press on behalf of the Royal Astronomical Society

al m

il,

454 G. Lodato et al.

Several questions arise, however, if one assumes a planetary origin for gaps in discs. In particular, gaps are typically observed at radial distances from the star of the order of 10-100 au (Zhang et al. 2016). It is therefore natural to ask how to reconcile this evidence with the lack of Jupiter-mass planets at such distances around mainsequence stars, as apparent from the extensive planet-detection campaigns of the last decade (Bowler & Nielsen 2018). In order to understand the orbital and physical evolution of planets from birth to adulthood, we need to compare the properties of planets around T Tauri stars and young stellar objects to those of planets around main-sequence stars. Such a comparison is not easy because usually the planet properties in gapped discs are obtained through complex and time-consuming numerical simulations, which are not feasible for large samples, and are sensitive to several physical parameters (dust-gas coupling, disc thermodynamics, etc.), for which specific assumptions need to be made.

In this paper, we provide an analysis of the properties of the newborn planet population, as implied from a sample of gaps and rings detected in our recent survey of discs in the Taurus-Auriga starforming region. To this end, we use a simple prescription to relate the observed width of the gap to the mass of planet assumed to be responsible for its opening. We then relate the resulting planetary properties to the stellar properties and to the population of known exo-planets.

This paper is organized as follows. In Section 2, we describe the simple method we use to give an estimate of the planet mass based on the gap morphologies. In Section 3, we show our main results. In Section 4, we draw our conclusions.

2 PLANET PROPERTIES FROM DISC GAPS

Recently, Long et al. (2018) investigated a subsample of 12 discs showing substructures within a larger sample of 32 discs in Taurus obtained with ALMA Band 6 (at 1.3 mm) in Cycle 4 (ID: 2016.1.01164.S; PI: Herczeg). The sample selection will be fully described by Long et al. (in preparation). Briefly, the sample was selected from stars in Taurus with spectral types earlier than M3 and with line-of-sight extinctions <3 mag. The selection was unbiased to the disc mm flux and to any previously known disc structures from mid-IR photometry; the primary bias is the exclusion of discs that had been previously imaged with ALMA at high spatial resolution. Some of these discs show multiple rings and gaps, providing us with a total of 15 gaps with known morphologies (excluding four additional discs with inner cavities). In Table 1, we provide a summary of the gap properties relevant to this study. A more detailed analysis can be found in Long et al. (2018).

Numerical simulations of gas and dust are the best tool to constrain the planetary properties that reproduce a given structure in a disc. However, such numerical simulations are very time consuming to determine the planetary properties for our sizable sample of discs. Instead, we use empirically determined scaling relations between the gap properties and the planetary mass. In particular, for low-viscosity discs ($\alpha \lesssim 0.01$), the gap width Δ (defined here as the distance between the location of the brightness minimum in the gap and the ring peak, see Long et al. 2018) is expected to scale with the planet Hill radius

$$R_{\rm H} = \left(\frac{M_{\rm p}}{3M_{\star}}\right)^{1/3} R,\tag{1}$$

where R is the planet position (assumed here to coincide with the gap location), with a proportionality constant ranging from 4 to 8 depending on the disc parameters, so that $\Delta = kR_{\rm H}$ (Dodson-

Robinson & Salyk 2011; Pinilla, Benisty & Birnstiel 2012; Fung & Chiang 2016; Rosotti et al. 2016; Facchini et al. 2018). Note that here we assume a one-to-one correspondence between a gap and a planet, while there is the possibility that multiple planets open a common single gap (Zhu et al. 2011) or that a single planet might open multiple gaps (Dong et al. 2018). Finally, note that the gap width likely depends somewhat on disc hydrodynamical properties, such as pressure and viscosity (Pinilla et al. 2012; Fung, Shi & Chiang 2014).

Two discs in our sample, MWC480 (Liu et al. 2019) and CI Tau (Clarke et al. 2018), have been simulated with detailed hydrodynamical simulations to reproduce the gap properties. MWC 480 presents a gap at \sim 73 au, which has been reproduced with a $2.3\,M_{\rm Jup}$ planet in the hydro simulations of Liu et al. (2019). The observed width of the gap in MWC 480 corresponds to $\sim 4.5 R_{\rm H}$. CI Tau presents three gaps at \sim 14, 48, and 120 au from the central star. Higher resolution observations of this system were obtained by Clarke et al. (2018), who model the three gaps with three planets with 0.75, 0.15, and 0.4 $M_{\rm Jup}$. It should be noted that the gap widths observed in Clarke et al. (2018) are not easily comparable to the ones measured by Long et al. (2018), due to the different functional form of the radial dust profile used and in particular due to the fact that Clarke et al. (2018) use different inner and outer gap width, as opposite to the symmetrical Gaussian employed in Long et al. (2018). Despite these differences, the two outermost gaps appear to have a comparable normalized width in the two studies, while the innermost one is much larger in Long et al. (2018) than in Clarke et al. (2018). This discrepancy is probably due to the limited spatial resolution of our observations compared to Clarke et al. (2018) (at the distance of CI Tau, 19 and 9 au, respectively) which is most important for the innermost ring, located at ~14 au. For consistency, in this paper we will always refer to the gap widths as measured by Long et al. (2018), keeping in mind that the width of the innermost gap in CI Tau might have been strongly overestimated.

The width of the two outer gaps in CI Tau corresponds to \sim 5 and 7 times the Hills radius of the planets used by Clarke et al. (2018) in their modelling. Thus, in the following, by averaging the results from hydrodynamical simulations of CI Tau and MWC 480, we will assume that the gap width Δ scales as

$$\Delta = 5.5 R_{\rm H}. \tag{2}$$

We remind the reader that the relation above is related to the gap in the dust radial profile, which may be different than the gas gap (which we do not consider in this paper). The resulting planet masses calculated with equation (2) for the 15 gaps in our sample are reported in Table 1.

The stellar masses are reproduced from those adopted by Long et al. (in preparation), obtained from a combination of dynamical mass measurements, when available (Simon, Dutrey & Guilloteau 2000; Piétu, Dutrey & Guilloteau 2007; Guilloteau et al. 2014; Simon et al. 2017), and otherwise by comparing literature estimates of temperature and luminosity to a combination of the Baraffe et al. (2015) and nonmagnetic models of Feiden (2016), as applied by Pascucci et al. (2016). UZ Tau E is a spectroscopic binary (e.g. Prato et al. 2002) and therefore has a dynamical mass that is much higher than would be expected from its spectral type.

In the plots shown below we also include error bars on the inferred planet masses coming from the uncertainty in the proportionality factor, ranging from 4.5 to 7 (Rosotti et al. 2016), resulting in an uncertainty in the inferred planet mass of the order of a factor \sim 2 either side, which dominates over the uncertainty on the assumed stellar mass.

al m

Cs

MNRAS 486, 453-461 (2019)

Table 1. Gap properties used in this study (from Long et al. 2018). The columns indicate, respectively: (1) star name; (2) gap width over gap location; (3) gap location with uncertainties from Long et al. (2018); (4) stellar mass; (5) total mm-flux at 1.3 mm of source; (6) total dust mass from mm-flux; and (7) inferred planet mass.

(1) Star name	(2) ∆/ <i>R</i>	(3) R/au	(4) M _* /M _⊙	(5) F / T	100 December 1	
RY Tau	0.129			(5) F_{ν}/mJy	(6) $M_{\rm dust}/M_{\rm Jup}$	$(7) M_p/M_{Jup}$
UZ Tau E	0.115	43.41 ± 0.13	$2.04^{+0.3}_{-0.26}$	210.39	0.29	0.077
DS Tau	0.724	69.05 ± 0.2	$1.23^{+0.08}_{-0.08}$	129.52	0.19	0.077
T Tau		32.93 ± 0.32	$0.83^{+0.02}_{-0.02}$	22.24	0.048	
/WC480	0.297	24.78 ± 0.19	$0.34^{+0.17}_{-0.09}$	89.77	0.12	5.6
ON Tau	0.329	73.43 ± 0.16	$2.1^{+0.06}_{-0.06}$	267.76	0.59	0.15
	0.083	49.29 ± 0.44	$0.87^{+0.17}_{-0.14}$	88.61		1.3
O Tau	0.239	58.91 ± 0.66	$0.49^{+0.01}_{-0.01}$	54.76	0.125	0.009
O Tau	0.258	86.99 ± 0.88	$0.49^{+0.01}_{-0.01}$	54.76	0.097	0.057
) Tau	0.171	41.15 ± 0.63	$0.74^{+0.01}_{-0.01}$	64.11	0.097	0.07
L Tau	0.182	39.29 ± 0.32	$1.02^{+0.02}_{-0.02}$		0.094	0.065
L Tau	0.166	66.95 ± 0.87	$1.02^{+0.02}_{-0.02}$	170.72	0.37	0.11
L Tau	0.262	88.9 ± 1.11	$1.02_{-0.02}^{+0.02}$ $1.02_{-0.02}^{+0.02}$	170.72	0.37	0.08
Tau	0.987	13.92 ± 0.32		170.72	0.37	0.33
Tau	0.281	48.36 ± 0.41	$0.91^{+0.02}_{-0.02}$	142.4	0.33	15.7
Tau	0.284	118.99 ± 0.65	$0.91^{+0.02}_{-0.02}$	142.4	0.33	0.36
		- 10.05 ± 0.05	$0.91^{+0.02}_{-0.02}$	142.4	0.33	0.37

Note that the outcome of hydrodynamical simulations of gas and dust with embedded planets depends on several physical and numerical parameters, including assumptions on the dustgas coupling, the detailed treatment of the gas thermodynamics (locally isothermal equations of state are often used), the use of twodimensional or three-dimensional codes, etc. All such assumptions imply an uncertainty in the relation between planet mass and width of the dust gap induced by it, often difficult to quantify. In this paper, we have simply assumed it to be given (see above) by the deviation between the different determination made by different groups using different codes and specific set-ups, although we warn that some of these uncertainties might be systematic (for example, most codes make the same assumptions on the thermodynamics, which may tend to overestimate the gap width for a given planet mass), and thus shared between all of the various simulations.

3 RESULTS

Fig. 1 shows a comparison between masses and locations of currently known exo-planets (empty circles, data from www.exopla net.eu, as of the 2018 Oct 31) and those inferred from the gap extents in Long et al. (2018) (red points) using equation (2). Recently, the DSHARP ALMA Large Program data have been released, with an analysis of additional gaps in bright protostellar discs. Zhang et al. (2018) measured the width¹ of 19 gaps, from which we calculate the putative planet mass with the same procedure as we used for the Long et al. (2018) sample, with stellar and disc parameters taken from Zhang et al. (2018). The resulting planet masses are shown with green points in Fig. 1 and are listed in Table 2. Despite the differences in estimating the planet masses, they appear to be consistent with those quoted by Zhang et al. (2018).

¹Note that Zhang et al. (2018) define the gap width in a slightly different way than us, so that $\Delta_{\rm Zhang}/R = (R_{\rm out} - R_{\rm in})/R_{\rm out}$, where $R_{\rm out, in}$ are the outer/inner radius of the gap, which makes their gap size of the order of two times the one obtained with our definition. When using their sample, we have corrected their data for this difference.

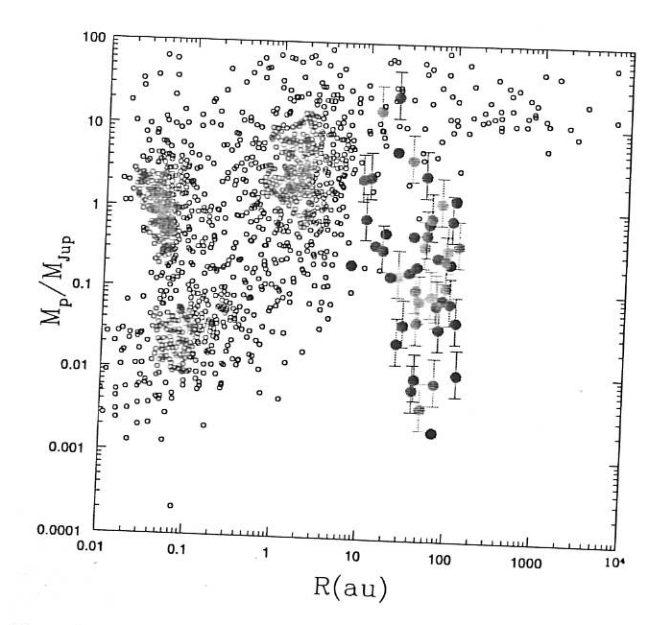


Figure 1. Plot of mass $(y-axis) M_p$ versus separation from the central star R(x-axis) of the (empty circles) currently known exo-planets (retrieved from the exoplanet.org data base) compared to those obtained from the sample in Long et al. (2018) (red points) and Zhang et al. (2018) (green points) using equation (2), and those collected by Bae et al. (2018) (blue points). Error bars in the planet masses indicate the uncertainty in the proportionality factor between gap width and planet's Hills radius, assumed to be in the range [4.5-7].

In addition, we also plot as blue circles the planet masses and locations inferred from other 14 ringed discs and disc hosting cavities (so-called transition discs), as collected by Bae, Pinilla & Birnstiel (2018) (see their Fig. 1). For the few cases (HD163296, Elias 24, and AS209) that are present both in the DSHARP and in the Bae et al. (2018) sample, we use the planet mass obtained from the measured gap width in DSHARP. We list the location and mass

MNRAS 486, 453-461 (2019)

Table 2. Planet masses for the gaps in the DSHARP survey (Zhang et al. 2018). The columns indicate, respectively: (1) star name; (2) gap width according to Zhang et al. (2018); (3) gap location; and (4) inferred planet mass.

(1) Star name	(2) Δ_{Zhang}/R	(3) <i>R</i> /au	$(4) M_{\rm p}/M_{\rm Jup}$
	0.42	9	2.25
AS209	0.31	99	0.74
AS209	0.32	57	0.77
Elias 24	0.18	69	0.07
Elias 27	0.15	74	0.035
GW Lup	0.13	16	0.3
HD 142666	0.62	22	23
HD 143006	0.22	51	0.48
HD 143006	0.24	10	0.74
HD 163296	0.34	48	2.5
HD 163296	0.17	86	0.23
HD 163296	0.45	- 11	2.4
SR4	0.15	98	0.07
DoAr 25	0.08	125	0.01
DoAr 25	0.13	25	0.02
Elias 20	0.13	117	0.04
IM Lup	0.13	29	0.038
RU Lup	0.14	39	0.006
Sz 114 Sz 129	0.08	41	0.008

Table 3. Planet masses collected by Bae et al. (2018). The columns indicate, respectively: (1) star name; (2) gap location; and (3) inferred planet mass.

	•	
(1) Star name	(2) <i>R</i> /au	(3) $M_{\rm p}/M_{\rm Jup}$
HL Tau	13.1	0.35
HL Tau	33	0.17
HL Tau	68.6	0.26
TW Hya	20	0.15
TW Hya	81	0.08
HD 169142	54	0.67
HD 97048	106	1.3
Lk Ca 15	36	0.47
RXJ 1615	97	0.22
	7	0.2
GY 91	40	0.2
GY 91	69	0.002
GY 91		0.5
V 4046	17	5
PDS 70	22	J

of the planets collected by Bae et al. (2018) in Table 3. In total, we thus have 48 planets inferred from the gaps in dusty discs, which is the largest gap sample analysed to date.

The inferred planet masses from our sample and the Zhang et al. (2018) sample are consistent with those of the Bae et al. (2018) sample, although we caution that the method used to derive them are significantly different: while the masses collected by Bae et al. (2018) are mostly inferred from hydrodynamical simulations, coupled with a dust evolution module, our estimates are based on a simpler approach. It is interesting to note, however, that the two approaches lead to compatible results.

The properties of the putative planets obtained with our method populate a region in the mass versus separation diagram that cannot be probed by the current exo-planet surveys. We note that the observations of planets at distances $\gtrsim 10$ au from the central star are biased towards large masses: at those separations planets can be detected mostly by direct imaging or by microlensing. Recent determinations of the occurrence rates of massive planets (M >

 $2\,M_{\rm Jup}$) beyond 10–20 au are in the range of a few up to 5 per cent (Bowler & Nielsen 2018). More specifically, the 68 per cent confidence interval is estimated to be [1.6–5.1] per cent for 2–14 $M_{\rm Jup}$ planets between 8 and 400 au by Lannier et al. (2016), [4–10] per cent for 5–20 $M_{\rm Jup}$ planets between 10 and 1000 au by Meshkat et al. (2017) and [0.75–5.7] per cent for 0.5–75 $M_{\rm Jup}$ between 20 and 300 au by Vigan et al. (2017). Note, however, that such estimates suffer from very large uncertainties, depending on whether one uses a hot or a cold start model for the planet. For example, Stone et al. (2018), using a cold start model, put an upper limit to the occurrence rate of 7–10 $M_{\rm Jup}$ planets between 5 and 50 au as high as 90 per cent for FGK stars.

For the combined sample, including the Long et al. (2018), Zhang et al. (2018), and Bae et al. (2018) data the occurrence rate of such massive planets is $7/48 \sim 15$ per cent, which is slightly higher than the published rates. However, note that, apart from the Long et al. (2018) sample, the other gap detections all present strong biases to very luminous mm sources. Furthermore, it is important to note that these planets will naturally accrete mass and migrate to the inner disc during their evolution, and thus change their properties, see Section 3.1.

From the planet-disc interaction point of view, the minimum planet-star mass ratio able to carve a dust gap depends on the coupling between the gas and the dust, as measured by the Stokes number

$$St = \Omega t_{stop}, \tag{3}$$

where t_{stop} is the drag stopping time and Ω is the local Keplerian frequency (Weidenschilling 1977). In particular, for strongly coupled dust grains (with St \ll 1) the minimum dust gap opening planet mass is

$$\frac{M_{\min}}{M_{\star}} = 0.3 \left(\frac{H}{R}\right)^3,\tag{4}$$

where *H/R* is the disc aspect ratio at the planet position, which depends on the disc temperature (Lambrechts, Johansen & Morbidelli 2014; Rosotti et al. 2016; Dipierro & Laibe 2017). If we consider a standard irradiated disc model (Chiang & Goldreich 1997; Dullemond, van Zadelhoff & Natta 2002; Armitage 2010), the disc aspect ratio is given by

$$\frac{H}{R} \approx 0.05 \left(\frac{R}{10 \text{ au}}\right)^{1/4}.$$
 (5)

In practice, since we obtain the planet mass from the gap width by assuming that it scales with the planet Hill's radius, the condition $M_p \gtrsim M_{\min}$ implies (through equations 1–4) that

$$\frac{\Delta}{R} \gtrsim [2.1 - 3.2] \frac{H}{R} \tag{6}$$

for strongly coupled dust, where the brackets correspond to our chosen interval in the proportionality factor in equation (1) (k = [4.5-7]). For more loosely coupled dust grains ($St \gtrsim 1$), conversely, a dust gap can be opened relatively more easily because viscous and pressure forces are not effective in closing the gap. Combining equations (56) and (58) in Dipierro & Laibe (2017), we obtain in this case the requirement:

$$\frac{\Delta}{R} \gtrsim \mathrm{St}^{-1/2} \frac{H}{R}.\tag{7}$$

Note that, for $St \le 1$ the gap width cannot be smaller than the disc thickness H.

al

M

y

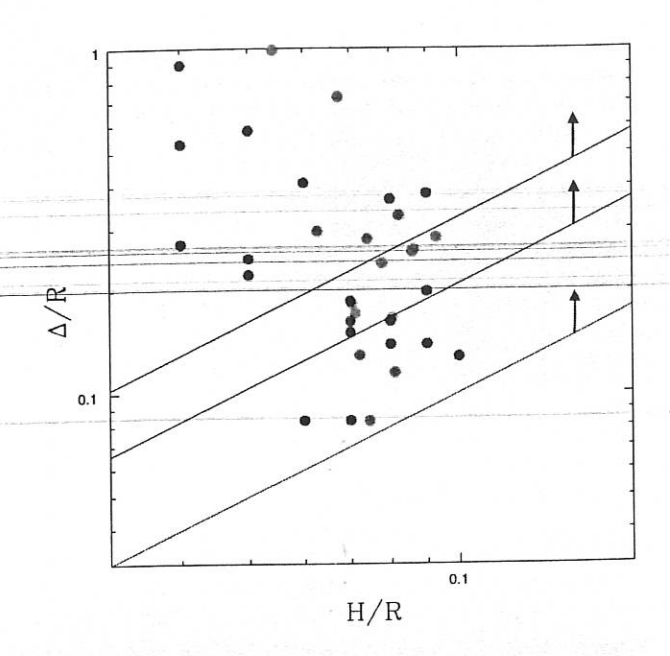


Figure 2. Measured gap widths versus disc aspect ratio (as estimated from equation 5) in the Long et al. (2018) (red points) and in the Zhang et al. (2018) (green points) samples. The two black lines indicate the range [2.1–3.2]H/R above which the gap width is expected to lie if the dust is strongly coupled to the gas (St \ll 1). The blue line indicates the relation $\Delta = H$, that is the minimum gap width expected for dust with St \sim 1.

In Fig. 2, we plot the gap width Δ/R for the gaps in the two samples of Long et al. (2018) (red points) and Zhang et al. (2018) (green points) versus the disc aspect ratio at the gap location H/R, as computed from equation (5). The two black lines indicate the range [2.1–3.2]H/R above which we should expect the gap width to lie, if the dust is strongly coupled to the gas. The blue line shows instead the simple relation $\Delta = H$, that is the minimum gap width expected for dust with St ~ 1 . As we can see, most of our points are consistent with the dust being strongly coupled to the gas. In a few cases the gap width appears to be somewhat smaller, which may imply that in these systems the dust is less coupled and it is thus easier to open up a dust gap.

Next, we check for possible correlations between the derived planet mass and the disc dust mass, as measured from the mm flux, assuming optically thin emission, a dust temperature of $T_{dust} = 20 \text{ K}$ and a dust opacity² $\kappa = 2.3 (v/230 \,\text{GHz})^{0.4} \,\text{cm}^2 \,\text{g}^{-1}$. This is plotted in Fig. 3, which shows the mass of the putative planets versus the total dust mass in the disc (Long et al. 2018). Apart from the two most massive planets (corresponding to the inner ring of CI Tau and to DS Tau), the rest of our small sample appears to follow a tentative trend. The solid line in Fig. 3 shows the best linear regression of the data (excluding the two outliers) in the form $M_p \propto M_{\rm dust}^{1.33}$. Note that, of course, this plot relates the planet mass to the current dust mass in the disc, which does not necessarily represent a proxy for the disc mass at the time of planet formation (Nixon, King & Pringle 2018). Moreover, inferring the value of the dust mass from continuum observations of protoplanetary discs is still under debate, mostly due to uncertainty in dust opacity and optical depth

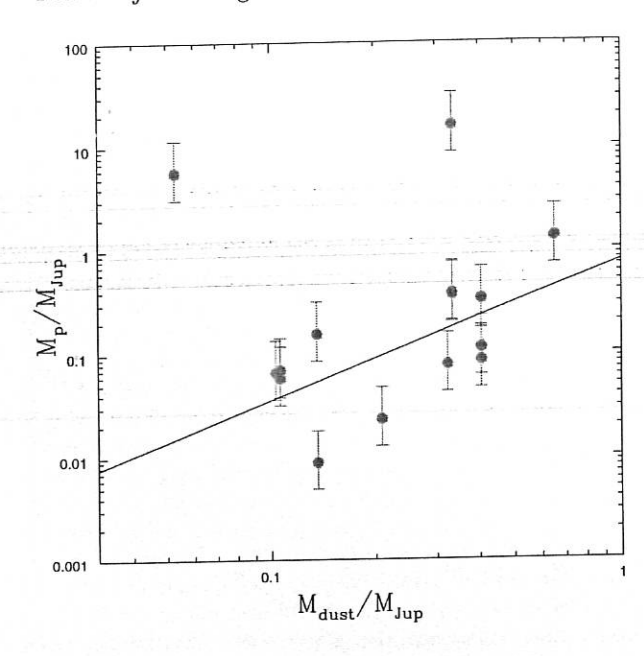


Figure 3. Mass of the planets M_p (y-axis) versus total dust mass in the disc (x-axis) for the putative planets in Long et al. (2018). The solid line indicates the linear regression of the form $M_p \propto M_{\rm dust}^{1.33}$.

(Bergin & Williams 2018). Indeed, Manara, Morbidelli & Guillot (2018), using photometric data, have recently shown that the disc dust masses measured from mm fluxes may be in general lower than the mass of exo-planets (but see Mulders, Pascucci & Apai 2015 and Pascucci et al. 2016 for a different opinion, based on Kepler planet mass estimates), as also confirmed by spatially resolved studies (Tazzari et al. 2017), who find dust surface density profiles below the Minimum Mass Solar Nebula in their Lupus disc sample. This can be explained with either a rapid formation of planetary cores (Najita & Kenyon 2014), or a replenishment of the disc from the environment, or a sizable fraction of circumstellar dust being captured in larger dust agglomerations such as boulders, planetesimals, etc. Especially for the two most massive inferred planets in our sample, it is possible that most of the primordial disc mass might have already ended up in planets that thus might appear to live in less massive discs than the correlation would suggest.

In a sample of transition discs, Pinilla et al. (2018) did not find any correlation between mm-flux and cavity size. Note that although also in transition discs the cavity is sometimes interpreted as the effect of the presence of a planet, here we are not concerned with discs with cavities, but only in gaps.

Finally, in Fig. 4 we show the location of the gaps in our sample versus the stellar masses. No clear trend can be recognized here, indicating that, in the planet interpretation, the planet formation region does not appear to depend strongly on the stellar mass.

3.1 The fate of planets

Due to interactions between planets and the surrounding disc material, the properties of the putative planets inferred in gappedlike discs around young stellar objects are expected to evolve with time. As a result, the planets would generally migrate and accrete mass from the surrounding disc.

In order to predict if the planets will survive to their migration and to compare their final properties with those of currently known exo-planets, we compute the variation of the separation and mass

MNRAS 486, 453-461 (2019)

m

² Although note that the dust opacity values are very uncertain, as it depends on the local size distribution and composition of dust grains, that is controlled by grain growth and radial drift.

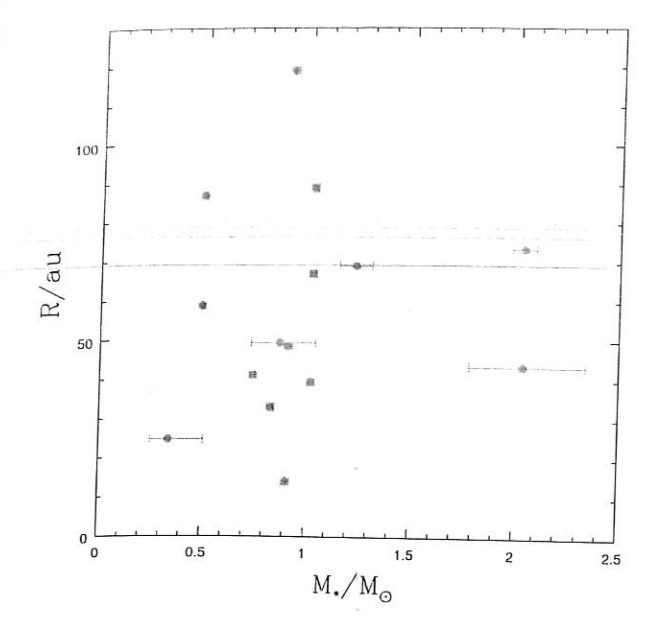


Figure 4. Scatter plot showing the gap location R (y-axis) versus the central star mass M_{\star} (x-axis) for the putative planets in Long et al. (2018).

of the planets under consideration using prescribed migration and accretion laws, assuming that the disc properties are fixed in time. We assume that the planets migrate according to type I or type II migration regime (e.g. see Papaloizou & Terquem 2006), depending on their ability to carve a deep gap in the local gas density structure (as opposed to the dust gaps that we know have been opened in all of our putative planets). Starting from the initial properties of the planets (see Tables 1–3), we assume that the gap-opening mass $M_{\rm p,gap}$ in the gas disc is given by the Crida, Morbidelli & Masset (2006) criterion, corresponding to a drop of the local gas surface density to a factor \sim 10 per cent of the unperturbed value, i.e.

$$\frac{3}{4} \frac{H}{R_{\rm H}} + \frac{50 \,\alpha M_{\star}}{M_{\rm p,gap}} \left(\frac{H}{R}\right)^2 = 1,\tag{8}$$

where α indicates the Shakura–Sunyaev turbulence parameter (Shakura & Sunyaev 1973), assumed to be equal to 0.005 (Flaherty et al. 2017). The value of the aspect ratio at the planet position is obtained from equation (5). We adopt a simplistic bimodal model for planetary migration by assuming that planets with mass smaller (larger) than $M_{\rm p,\,gap}$ migrate according to type I (II) regime.

The planet orbital evolution and accretion history are then computed following the method of Dipierro et al. (2018) (see their section 4.4 for details). In particular, we assume that low-mass planets (i.e. $M_p < M_{p,\,\rm gap}$) initially undergo a rapid growth and migration phase (corresponding to the Type I regime, when the planet is still embedded in the disc), rapidly reaching a mass and radius given by equations (20)–(22) in Dipierro et al. (2018). Then, we let the planets migrate without growing in mass on the slower viscous time-scale of the disc:

$$t_{\text{migr,II}} = \frac{2}{3} \left(\frac{1}{\alpha \Omega} \right) \left(\frac{H}{R} \right)^{-2}.$$
 (9)

Those planets in our sample with an initially high mass (i.e. $M_{\rm p}$ > $M_{\rm p,\,gap}$) simply migrate towards the central star according to the type II regime. If the planet mass is much larger than the local disc mass, Type II migration is expected to be further slowed down by a factor $B=M_{\rm p}/4\pi~\Sigma~R^2$, where Σ is the total (gas + dust) disc surface

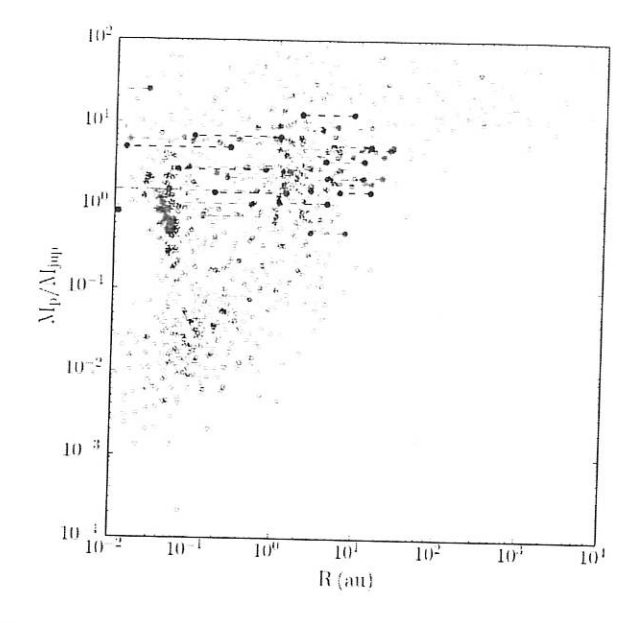


Figure 5. Same as Fig. 1 but where the points indicate the expected final mass and location of the putative planets inferred in Long et al. (2018) (red), Zhang et al. (2018) (green), and Bae et al. (2018) (blue) after 3 and 5 Myr of planet evolution. The dashed lines indicate the range of planet locations after a total time in the range [3,5] Myr. Planetary accretion and migration lead to a redistribution of planet properties that mostly populates the branch of cold Jupiters.

density (Ivanov, Papaloizou & Polnarev 1999). However, given that the dust masses for our sample (see Table 1) are generally of the order of the estimated planet mass, and assuming a gas-to-dust ratio of 100, we find that none of our planets is massive enough to be in this modified Type II migration regime.

Fig. 5 shows the final properties (separation from the central star and mass) of the planets in our sample. The dashed lines indicate the range of planet locations after a total time in the range [3,5] Myr (taken to be an estimate of the gas disc lifetime, including a possible spread in ages and evolutionary time), compared to those inferred from the currently known exo-planets. Initially, around half of the planets in our sample have a mass below the one given by the gas gap-opening criterion and therefore accrete mass and migrate in type I regime. We find that these migrating and accreting planets will reach the gap opening mass (equation 8) and transit into the slow type II migration regime well before being lost into the central star (and thus save themselves from rapid migration), consistently with recent findings of Crida & Bitsch (2017) and Johansen, Ida & Brasser (2018). More massive planets (i.e. $M_p > M_{p,gap}$) simply slowly migrate towards the central star according to the type II regime. After planetary migration and accretion, ~20 per cent of the planets are lost into the star (we assume that a planet is lost into the star if its separation is smaller than 0.01 au). Moreover, nearly all of the planets in our sample reach a mass above Jupiter.

Our evolutionary model is very simplified and approximated: we have kept the disc properties fixed during the evolution, we have simply assumed a uniform lifetime for all the discs (neglecting also a possible range in ages in our sample) and we have neglected possible modifications to the migration laws (e.g. Ivanov et al. 1999; Dürmann & Kley 2015). However, it is interesting to note that the final distribution of the planets is consistent with the known properties of the exo-planet population, especially those placed in the branch of cold Jupiters.

Cel

M

Ca

MNRAS 486, 453–461 (2019)

Lf

Since the planetary growth and migration are closely linked to the disc evolution, a proper investigation should take into account the underlying evolution of the dynamical and thermal structure of the gas and dust content in protoplanetary discs, along with the possible presence of mechanisms acting to slow-down (or even reverse) the inward planet migration such as photoevaporation (Matsuyama, Johnstone & Murray 2003; Alexander & Pascucci 2012), migration in a multiple planet system (Martin et al. 2007), disc migration feedback (Fung & Lee 2018), sublimation lines, shadowed regions and heat transition barriers (e.g. Bitsch et al. 2015; Baillié, Charnoz & Pantin 2016; Johansen et al. 2018; Ndugu, Bitsch & Jurua 2018), and even further migration occurring by planet–planet interaction after the disc is dispersed.

4 CONCLUSIONS

In this paper, we have analysed the sample of rings and gaps observed to date in protoplanetary discs to infer the properties of the population of planets that might have been able to carve the observed gaps. Our analysis includes the recent detections of gaps in discs in the Taurus star-forming region by Long et al. (2018), along with the recent observations in the DSHARP ALMA Large Program analysed by Zhang et al. (2018) and the additional sample of gaps collected by Bae et al. (2018). For those discs where a proper hydrodynamical modelling was not carried out to infer the planet properties, we estimate the putative planet masses assuming that the gap width is proportional to the planet Hill's radius. We then describe some possible correlations of the putative planet properties with the other system parameters.

The most important conclusion of our work is that there appears to be no discrepancy between the possibility that embedded planets are responsible for carving gaps in discs around young stars and the lack of detections at similar locations by dedicated planet searches. First, we find that the locations and masses of the planets around these young stars occupy a distinct region in the planet mass versus semimajor axis plane that is presently not probed by planet detection campaigns (around both young, T Tauri stars and older, mainsequence stars). The high frequency of gaps observed in planet forming discs has sometimes been interpreted as evidence against a planet induced model for gap formation, based on the fact that planet detection campaigns do not observe massive planets at tens of au very frequently. Our analysis, however, shows that if the planets remain at the lower end of the masses required to create gaps then they would be, as yet, undetectable by campaigns searching at these distances.

The number of gaps in the sample of Long et al. (2018) (which is the least biased sample of gaps in discs available so far) is 15 out of 32 targets. Taking into account the fraction of disc hosting stars in Taurus, which is 0.75 (Luhman et al. 2010), this leads to an occurrence rate of gaps around young stars of 35 per cent. Fernandes et al. (2019) have compared favourably this number with their estimate of the number of giant planets (with masses in the $[0.1-20]\,M_{\rm Jup}$ range and semimajor axis in the $[0.1-100]\,$ au range), which is 26.6 per cent. A similar occurrence rate from RV surveys has also been published by Cumming et al. (2008), who estimate a value of 17–20 per cent for giant planets (above Saturn mass) within 20 au. However, one must remember that the occurrence rates of giant planets from RV surveys or direct imaging should not be directly compared with the occurrence rates of gaps, because planets migrate and accrete mass during the disc evolution.

Motivated by this, we further explore the final properties of the planets in our sample by using a simple prescription of planetary migration and accretion (Dipierro et al. 2018). After 3–5 Myr of planetary evolution, we find that the final properties of the planets approach the branch of cold Jupiters in the current observed distribution of exoplanets. Thus, planetary migration and accretion provide a second explanation for the lack of detected planets at large distances around older, main-sequence stars.

After planetary migration and accretion, ~20 per cent of the planets are lost into the star. However, for the subsample including only Long et al. (2018) discs, only one planet is lost and the final number of surviving planets is 14, most of them having masses above Jupiter. In total, thus, the occurrence rate of Jupiter mass planets in our model is 33 per cent. As mentioned above, Fernandes et al. (2019) estimate a value of 26.6 per cent for the occurrence rate of giants (with masses above $0.1 M_{Jup}$), but this number is reduced to only 6 per cent for Jupiter mass planets, according to Fernandes et al. (2019). This interesting fact can be explained in several different ways. First, we note that our estimates are certainly affected with low-number statistic uncertainties, and future, unbiased larger surveys should improve in this respect. Secondly, it is worth noting that planet detection campaigns concentrate on Solar type stars, while this is not the case for the disc surveys, which include a wider range of stellar types. Thirdly, our planetary accretion model probably overestimates the amount of accreted mass. Indeed, we assume an isothermal equation of state to compute the accretion rate (Dipierro et al. 2018), which is the maximum accretion rate allowed (Ayliffe & Bate 2009; Szulágyi 2015; Szulágyi et al. 2016; Lambrechts & Lega 2017). Certainly, this kind of comparison can put interesting constraints on accretion and migration models.

Estimating the presence of a planet based on the gap it carves in the protoplanetary disc naturally has a bias in that very low mass planets do not induce gaps. Such a bias can be quantified using known relationships between the minimum gap opening planet mass (and thus the minimum expected gap width) and the disc aspect ratio. Our results show that the measured gap widths are generally larger than a few times the disc thickness H, which is consistent with predictions for planet gap opening for a dust population strongly coupled to the gas. In a few cases, the gap width is comparable to H, which might imply that the dust–gas coupling in these systems is lower. However, these gaps are still consistent with $St \gtrsim 1$ for the mm-sized grains, as required for them to remain at their current location and not undergo rapid inward drift. In no cases do we find gap widths smaller than H, which strongly supports our hypothesis that the observed gaps are opened by planets.

Despite uncertainties coming from the small size of our sample (and by the presence of a couple of outliers), we suggest that there could be a correlation between planet mass and disc mass, as inferred from the disc mm flux, supporting the notion that more massive discs tend to produce more massive planets. However, note that a similar correlation between mm flux and cavity size was not found for the larger cavities (as opposed to the gaps discussed here) around transition discs, analysed by Pinilla et al. (2018). No correlation is instead found between the location of the gaps and the stellar mass, possibly indicating that the planet formation region does not appear to depend strongly on stellar mass, although again note that this might be affected by the relatively small sample size.

Upcoming surveys of discs will certainly add more data points to our currently small sample and further refine or reject our findings. Importantly, theoretical models have developed to the point of making a priori predictions for exo-planet demographics. In general, analyses such as ours, once the samples are more complete, will be needed to relate the properties of newborn planets with the 'adult'

MNRAS 486, 453-461 (2019)

m

(9)

Feiden G. A., 2016, A&A, 593, A99

Fernandes R. B., Mulders G. D., Pascucci I., Mordasini C., Emsenhuber A., 2019, ApJ, 874, 81

Flaherty K. M. et al., 2017, ApJ, 843, 150

Fung J., Chiang E., 2016, ApJ, 832, 105

Fung J., Lee E. J., 2018, ApJ, 859, 126

Fung J., Shi J.-M., Chiang E., 2014, ApJ, 782, 88

Gonzalez J.-F., Laibe G., Maddison S. T., Pinte C., Ménard F., 2015, MNRAS, 454, L36

Guilloteau S., Simon M., Piétu V., Di Folco E., Dutrey A., Prato L., Chapillon E., 2014, A&A, 567, A117

Hendler N. P. et al., 2018, MNRAS, 475, L62

Huang J. et al., 2018, ApJ, 869, L42

Isella A. et al., 2016, Phys. Rev. Lett., 117, 251101

Ivanov P. B., Papaloizou J. C. B., Polnarev A. G., 1999, MNRAS, 307, 79

Johansen A., Ida S., Brasser R., 2019, A&A, 622, A202

Lambrechts M., Lega E., 2017, A&A, 606, A146

Lambrechts M., Johansen A., Morbidelli A., 2014, A&A, 572, A35

Lannier J. et al., 2016, A&A, 596, A83

Liu Y. et al., 2019, A&A, 622, A75

Long F. et al., 2018, ApJ, 869, 17

Luhman K. L., Allen P. R., Espaillat C., Hartmann L., Calvet N., 2010, ApJS, 186, 111

Manara C. F., Morbidelli A., Guillot T., 2018, A&A, 618, L3

Martin R. G., Lubow S. H., Pringle J. E., Wyatt M. C., 2007, MNRAS, 378,

Matsuyama I., Johnstone D., Murray N., 2003, ApJ, 585, L143

Meshkat T. et al., 2017, AJ, 154, 245

Mulders G. D., Pascucci I., Apai D., 2015, ApJ, 814, 130

Najita J. R., Kenyon S. J., 2014, MNRAS, 445, 3315

Ndugu N., Bitsch B., Jurua E., 2018, MNRAS, 474, 886

Nixon C. J., King A. R., Pringle J. E., 2018, MNRAS, 477, 3273 Papaloizou J. C. B., Terquem C., 2006, Rep. Prog. Phys., 69, 119

Pascucci I. et al., 2016, ApJ, 831, 125

Piétu V., Dutrey A., Guilloteau S., 2007, A&A, 467, 163

Pinilla P. et al., 2018, ApJ, 859, 32

Pinilla P., Benisty M., Birnstiel T., 2012, A&A, 545, A81

Prato L., Simon M., Mazeh T., Zucker S., McLean I. S., 2002, Ap.I., 579,

Rosotti G. P., Juhasz A., Booth R. A., Clarke C. J., 2016, MNRAS, 459,

Ruge J. P., Flock M., Wolf S., Dzyurkevich N., Fromang S., Henning T., Klahr H., Meheut H., 2016, A&A, 590, A17

Shakura N. I., Sunyaev R. A., 1973, A&A, 24, 337

Simon M. et al., 2017, ApJ, 844, 158

Simon M., Dutrey A., Guilloteau S., 2000, ApJ, 545, 1034

Stone J. M. et al., 2018, A.I, 156, 286

Suriano S. S., Li Z.-Y., Krasnopolsky R., Shang H., 2018, MNRAS, 477, 1239

Szulágyi J., 2015, PhD thesis. Univ. Nice Sophia Antipolis

Szulágyi J., Masset F., Lega E., Crida A., Morbidelli A., Guillot T., 2016, MNRAS, 460, 2853

Tazzari M. et al., 2017, A&A, 606, A88

van Terwisga S. E. et al., 2018, A&A, 616, A88

Vigan A. et al., 2017, A&A, 603, A3

Weidenschilling S. J., 1977, MNRAS, 180, 57

Zhang S. et al., 2018, Ap.J, 869, L47

Zhang K., Blake G. A., Bergin E. A., 2015, ApJ, 806, L7

Zhang K., Bergin E. A., Blake G. A., Cleeves L. I., Hogerheijde M., Salinas V., Schwarz K. R., 2016, ApJ, 818, L16

Zhu Z., Nelson R. P., Hartmann L., Espaillat C., Calvet N., 2011, ApJ, 729,

evolution of planets in their discs.

ACKNOWLEDGEMENTS

We thank an anonymous referee for their insightful comments. We thank Jaehan Bae for providing us with masses and separations from the central star collected in Bae et al. (2018). GL, ERa, BN, and ERi acknowledge support by the project PRIN-INAF 2016 The Cradle of Life - GENESIS-SKA (General Conditions in Early Planetary Systems for the rise of life with SKA). This project has received funding from the European Union's Horizon 2020 research and innovation programme under the Marie Sklodowska-Curie grant agreement No 823823 (Dustbusters RISE project). GD and ERa acknowledge financial support from the European Research Council (ERC) under the European Union's Horizon 2020 research and innovation programme (grant agreement No 681601). MT has been supported by the DISCSIM project, grant agreement 341137 funded by the European Research Council under ERC-2013-ADG and by the UK Science and Technology research Council (STFC). DJ is supported by the National Research Council of Canada and by an NSERC Discovery Grant. FMe, GvdP, YB acknowledge funding from ANR of France (contract ANR-16-CE31-0013, Planet-Forming-Discs). FL and GJH are supported by general grants 11773002 and 11473005 awarded by the National Science Foundation of China. CFM acknowledges an ESO Fellowship and was partly supported by the Deutsche Forschungs-Gemeinschaft (DFG, German Research Foundation) - Ref no. FOR 2634/1 TE 1024/1-1, by the DFG cluster of excellence Origin and Structure of the Universe (www.universe-cluster.de).

main-sequence stars, thus posing important constraints on the early

REFERENCES

Alexander R. D., Pascucci I., 2012, MNRAS, 422, L82

ALMA Partnership et al., 2015, ApJL, 808, L3

Andrews S. M. et al., 2016, ApJ, 820, L40

Armitage P. J., 2010, Astrophysics of Planet Formation. Cambridge Univ. Press, Cambridge

Ayliffe B. A., Bate M. R., 2009, MNRAS, 393, 49

Bae J., Pinilla P., Birnstiel T., 2018, ApJ, 864, L26

Baillié K., Charnoz S., Pantin E., 2016, A&A, 590, A60

Baraffe I., Homeier D., Allard F., Chabrier G., 2015, A&A, 577, A42 Barge P., Ricci L., Carilli C. L., Previn-Ratnasingam R., 2017, A&A, 605,

A122

Bergin E. A., Williams J. P., 2018, preprint (arXiv:1807.09631)

Bitsch B., Joha sen A., Lambrechts M., Morbidelli A., 2015, A&A, 575, A28

Bowler B. P., Nielsen E. L., 2018, in Deeg H., Belmonte J., eds, Handbook of exoplanets. Springer, Cham, 155

Chiang E. I., Goldreich P., 1997, ApJ, 490, 368

Clarke C. J. et al., 2018, ApJ, 866, L6

Crida A., Bitsch B., 2017, Icarus, 285, 145

Crida A., Morbidelli A., Masset F., 2006, Icarus, 181, 587

Cumming A., Butler R. P., Marcy G. W., Vogt S. S., Wright J. T., Fischer D. A., 2008, PASP, 120, 531

Dipierro G. et al., 2018, MNRAS, 475, 5296

Dipierro G., Laibe G., 2017, MNRAS, 469, 1932

Dipierro G., Price D., Laibe G., Hirsh K., Cerioli A., Lodato G., 2015, MNRAS, 453, L73

Dodson-Robinson S. E., Salyk C., 2011, ApJ, 738, 131

Dong R., Li S., Chiang E., Li H., 2018, ApJ, 866, 110

Dullemond C. P., van Zadelhoff G. J., Natta A., 2002, A&A, 389, 464

Dürmann C., Kley W., 2015, A&A, 574, A52

)

- ¹Dipartimento di Fisica, Università degli Studi di Milano, Via Celoria 16, I-20133 Milano, Italy
- ²Department of Physics and Astronomy, University of Leicester, Leicester LEI 7RH, UK
- ³Kavli Institute for Astronomy and Astrophysics, Peking University, Yiheyuan 5, Haidian Qu, 100871 Beijing, China
- ⁴Lunar and Planetary Laboratory, University of Arizona, Tucson, AZ 85721, USA
- ⁵Earths in Other Solar Systems Team, NASA Nexus for Exoplanet System Science, USA
- ⁶Department of Astronomy/Steward Observatory, The University of Arizona, 933 North Cherry Avenue, Tucson, AZ 85721, USA
- ⁷European Southern Observatory, Karl-Schwarzschild-Str. 2, D-85748
- Garching bei München, Germany

 8 Institute of Astronomy, University of Cambridge, Madingley Road, Cam-
- bridge CB3 0HA, UK

 Max Planck Institute for Astronomy, Königstuhl 17, D-69117 Heidelberg,
- ¹⁰Purple Mountain Observatory & Key Laboratory for Radio Astronomy, Chinese Academy of Sciences, 2 West Beijing Road, Nanjing 210008,
- ¹¹Department of the Geophysical Sciences, The University of Chicago, Chicago, IL 60637, USA

- ¹²Leiden Observatory, Leiden University, P.O. box 9513, NL-2300 RA Leiden, The Netherlands
- 13 Univ. Grenoble Alpes, CNRS, IPAG, F-38000 Grenoble, France
- ¹⁴NRC Herzberg Astronomy and Astrophysics, 5071 West Saanich Road, Victoria, BC V9E 2E7, Canada
- ¹⁵Department of Physics and Astronomy, University of Victoria, Victoria, BC, V8P 5C2, Canada
- ¹⁶ Vassar College Physics and Astronomy Department, 124 Raymond Avenue, Poughkeepsie, NY 12604, USA
- ¹⁷Sorbonne Université, Observatoire de Paris, Université PSL, CNRS, LERMA, F-75014 Paris, France
- ¹⁸ Five College Astronomy Department, Smith College, Northampton, MA 01063, USA
- ¹⁹Space Telescope Science Institute Baltimore, MD 21218, USA
- ²⁰INAF-Osservatorio Astronomico di Roma, via di Frascati 33, I-00040 Monte Porzio Catone, Italy
- ²¹INAF-Osservatorio Astronomico di Padova, Vicolo dell'Osservatorio 5, I-35122 Padova, Italy
- ²²NASA Ames Research Center and Bay Area Environmental Research Institute, Moffett Field, CA 94035, USA

This paper has been typeset from a TEX/LETEX file prepared by the author.

al

MNRAS 486, 453–461 (2019)

m /

Measurement of matter-antimatter differences in beauty baryon decays

The LHCb collaboration[†]

Differences in the behaviour of matter and antimatter have been observed in K and B meson decays, but not yet in any baryon decay. Such differences are associated with the non-invariance of fundamental interactions under the combined charge-conjugation and parity transformations, known as CP violation. Here, using data from the LHCb experiment at the Large Hadron Collider, we search for CP-violating asymmetries in the decay angle distributions of Λ_b^0 baryons decaying to $p\pi^-\pi^+\pi^-$ and $p\pi^-K^+K^-$ final states. These four-body hadronic decays are a promising place to search for sources of CP violation both within and beyond the standard model of particle physics. We find evidence for CP violation in Λ_b^0 to $p\pi^-\pi^+\pi^-$ decays with a statistical significance corresponding to 3.3 standard deviations including systematic uncertainties. This represents the first evidence for CP violation in the baryon sector.

he asymmetry between matter and antimatter is related to the violation of the CP symmetry (CPV), where C and P are the charge-conjugation and parity operators. CP violation is accommodated in the standard model (SM) of particle physics by the Cabibbo-Kobayashi-Maskawa (CKM) mechanism that describes the transitions between up- and down-type quarks^{1,2}, in which quark decays proceed by the emission of a virtual W boson and where the phases of the couplings change sign between quarks and antiquarks. However, the amount of CPV predicted by the CKM mechanism is not sufficient to explain our matter-dominated Universe3,4 and other sources of CPV are expected to exist. The initial discovery of CPV was in neutral K meson decays5, and more recently it has been observed in B^0 (refs 6,7), B^+ (refs 8–11), and B_s^0 (ref. 12) meson decays, but it has never been observed in the decays of any baryon. Decays of the Λ_h^0 (bud) baryon to final states consisting of hadrons with no charm quarks are predicted to have non-negligible CP asymmetries in the SM, as large as 20% for certain three-body decay modes13. It is important to measure the size and nature of these CP asymmetries in as many decay modes as possible, to determine whether they are consistent with the CKM mechanism or, if not, what extensions to the SM would be required to explain them¹⁴⁻¹⁶.

The decay processes studied in this article, $\Lambda_b^0 \to p\pi^-\pi^+\pi^-$ and $\Lambda_b^0 \to p\pi^-K^+K^-$, are mediated by the weak interaction and governed mainly by two amplitudes, expected to be of similar magnitude, from different diagrams describing quark-level $b \to u\overline{u}d$ transitions, as shown in Fig. 1. Throughout this paper the inclusion of charge-conjugate reactions is implied, unless otherwise indicated. CPV could arise from the interference of two amplitudes with relative phases that differ between particle and antiparticle decays, leading to differences in the Λ_b^0 and $\overline{\Lambda}_b^0$ decay rates. The main source of this effect in the SM would be the large relative phase (referred to as α in the literature) between the product of the CKM matrix elements $V_{ub}V_{ud}^*$ and $V_{tb}V_{ud}^*$, which are present in the different diagrams depicted in Fig. 1. Parity violation (PV) is also expected in weak interactions, but has never been observed in Λ_b^0 decays.

To search for CP-violating effects one needs to measure CP-odd observables, which can be done by studying asymmetries in the \widehat{T} operator. This is a unitary operator that reverses both the momentum and spin three-vectors^{17,18}, and is different from the antiunitary time-reversal operator $T^{19,20}$ that also exchanges

initial and final states. A non-zero CP-odd observable implies CP violation, and similar considerations apply to P-odd observables and parity violation²¹. Furthermore, different values of P-odd observables for a decay and its charge conjugate would imply CPV. In this paper, scalar triple products of final-state particle momenta in the Λ_b^0 centre-of-mass frame are studied to search for P- and CP-violating effects in four-body decays. These are defined as $C_{\widehat{T}} = \mathbf{p}_p \cdot (\mathbf{p}_{h_1^+} \times \mathbf{p}_{h_2^+})$ for Λ_b^0 where h_1 and h_2 are final-state hadrons: $h_1 = \pi$ and $h_2 = K$ for $\Lambda_b^0 \to p\pi^-K^+K^-$ and $h_1 = h_2 = \pi$ for $\Lambda_b^0 \to p\pi^-\pi^+\pi^-$. In the latter case there is an inherent ambiguity in the choice of the pion for h_1 that is resolved by taking that with the larger momentum in the Λ_b^0 rest frame, referred to as π_{fast} . The following asymmetries may then be defined 22,23 :

$$A_{\widehat{T}}(C_{\widehat{T}}) = \frac{N(C_{\widehat{T}} > 0) - N(C_{\widehat{T}} < 0)}{N(C_{\widehat{T}} > 0) + N(C_{\widehat{T}} < 0)}$$
(1)

$$\overline{A}_{\widehat{T}}(\overline{C}_{\widehat{T}}) = \frac{\overline{N}(-\overline{C}_{\widehat{T}} > 0) - \overline{N}(-\overline{C}_{\widehat{T}} < 0)}{\overline{N}(-\overline{C}_{\widehat{T}} > 0) + \overline{N}(-\overline{C}_{\widehat{T}} < 0)}$$
(2)

where N and \overline{N} are the numbers of Λ_b^0 and $\overline{\Lambda}_b^0$ decays. These asymmetries are P-odd and \widehat{T} -odd and so change sign under P or \widehat{T} transformations, that is, $A_{\widehat{T}}(C_{\widehat{T}}) = -A_{\widehat{T}}(-C_{\widehat{T}})$ or $\overline{A}_{\widehat{T}}(\overline{C}_{\widehat{T}}) = -\overline{A}_{\widehat{T}}(-\overline{C}_{\widehat{T}})$. The P- and CP-violating observables are defined as

$$a_p^{\widehat{\tau}\text{-odd}} = \frac{1}{2} \left(A_{\widehat{\tau}} + \overline{A}_{\widehat{\tau}} \right), \qquad a_{CP}^{\widehat{\tau}\text{-odd}} = \frac{1}{2} \left(A_{\widehat{\tau}} - \overline{A}_{\widehat{\tau}} \right)$$
 (3)

and a significant deviation from zero would signal PV or CPV, respectively.

Searches for CPV with triple-product asymmetries are particularly suited to Λ_b^0 four-body decays to hadrons with no charm quark²⁴ thanks to the rich resonant substructure, dominated by $\Delta(1232)^{++} \to p\pi^+$ and $\rho(770)^0 \to \pi^+\pi^-$ resonances in the $\Lambda_b^0 \to p\pi^-\pi^+\pi^-$ final state. The observable $a_{CP}^{\widehat{T}\text{-odd}}$ is sensitive to the interference of \widehat{T} -even and $\widehat{T}\text{-odd}$ amplitudes with different CP-odd ('weak') phases. Unlike the overall asymmetry in the decay race that is sensitive to the interference of $\widehat{T}\text{-even}$ amplitudes, $a_{CP}^{\widehat{T}\text{-odd}}$ does not require a non-vanishing difference

ghts reserved.

as Uf

 $^{^{\}dagger}$ A full list of authors and affiliations appears at the end of the paper.

APOLICE

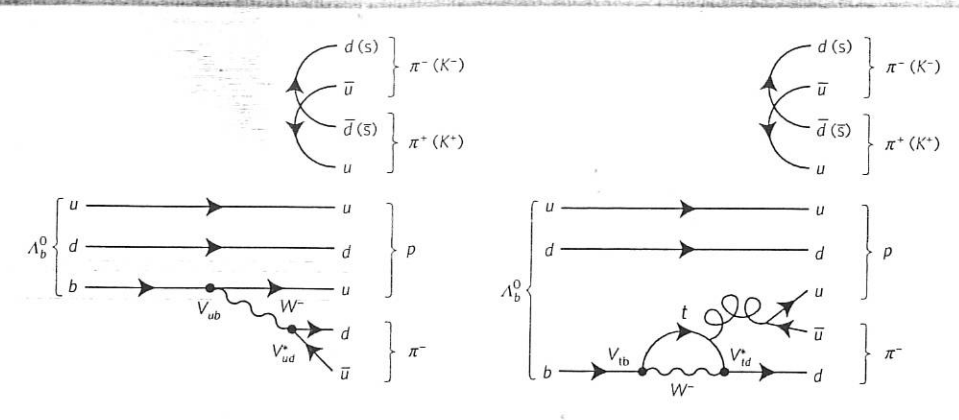


Figure 1 | Dominant Feynman diagrams for $\Lambda_b^0 \to p\pi^-\pi^+\pi^-$ and $\Lambda_b^0 \to p\pi^-K^+K^-$ transitions. The two diagrams show the transitions that contribute most strongly to $\Lambda_b^0 \to p\pi^-\pi^+\pi^-$ and $\Lambda_b^0 \to p\pi^-K^+K^-$ decays. In both cases, a pair of $\pi^+\pi^-$ (K^+K^-) is produced by gluon emission from the light quarks (u,d). The difference is in the b quark decay that happens on the left through a virtual W^- boson emission ('tree diagram') and on the right as a virtual W^- boson emission and absorption together with a gluon emission ('loop diagram'). The magnitudes of the two amplitudes are expected to be comparable, and each is proportional to the product of the CKM matrix elements involved, which are shown in the figure.

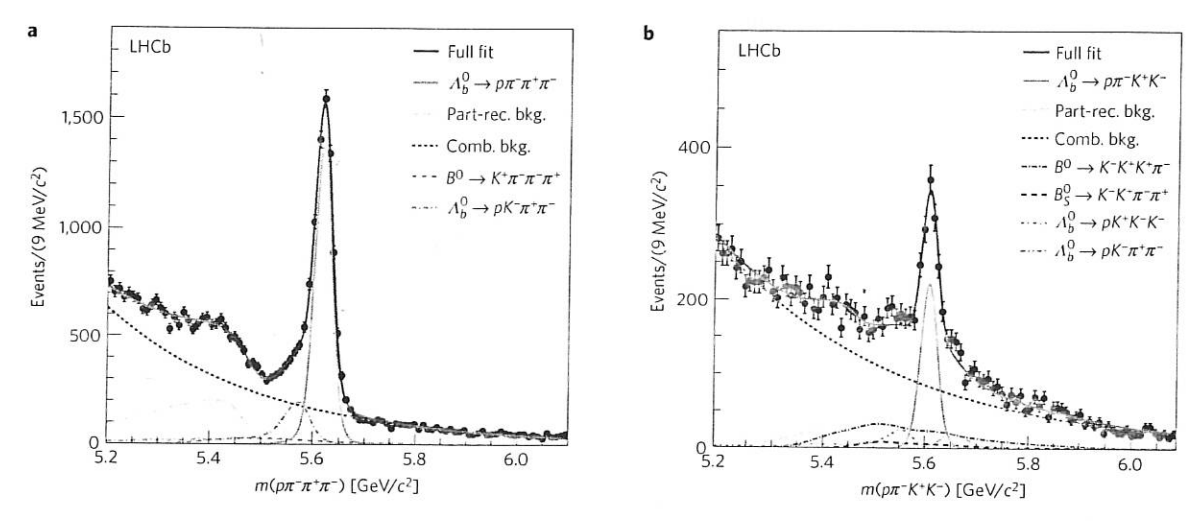


Figure 2 | Reconstructed invariant mass fits used to extract the signal yields. The invariant mass distributions for (a) $\Lambda_b^0 \to \rho \pi^- \pi^+ \pi^-$ and (b) $\Lambda_b^0 \to \rho \pi^- K^+ K^-$ decays are shown. A fit is overlaid on top of the data points, with solid and dotted lines describing the projections of the fit results for each of the components described in the text and listed in the legend. Uncertainties on the data points are statistical only and represent one standard deviations, calculated assuming Poisson-distributed entries.

in the CP-invariant ('strong') phase between the contributing amplitudes^{19,25}. The observables $A_{\widehat{T}}$, $\overline{A}_{\widehat{T}}$, $a_P^{\widehat{T}\text{-odd}}$ and $a_{CP}^{\widehat{T}\text{-odd}}$ are, by construction, largely insensitive to particle–antiparticle production asymmetries and detector-induced charge asymmetries²⁶.

This article describes measurements of the CP- and P-violating asymmetries introduced in equation (3) in $\Lambda_b^0 \to p\pi^-\pi^+\pi^-$ and $\Lambda_b^0 \to p\pi^-K^+K^-$ decays. The asymmetries are measured first for the entire phase space of the decay, integrating over all possible final-state configurations, and then in different regions of phase space so as to enhance sensitivity to localized CPV. The analysis is performed using proton–proton collision data collected by the LHCb detector, corresponding to 3.0 fb⁻¹ of integrated luminosity at centre-of-mass energies of 7 and 8 TeV, and exploits the copious production of Λ_b^0 baryons at the LHC, which constitutes around 20% of all b hadrons produced²⁷. Control samples of $\Lambda_b^0 \to pK^-\pi^+\pi^-$ and $\Lambda_b^0 \to \Lambda_c^+\pi^-$ decays, with Λ_c^+ decaying to $pK^-\pi^+$, $p\pi^-\pi^+$, and pK^-K^+ final states, are used to optimize the event selection and study systematic effects; the most abundant control sample consists of $\Lambda_b^0 \to \Lambda_c^+(pK^-\pi^+)\pi^-$ decays mediated by $b \to c$ quark transitions in which no CPV is expected²⁸. To avoid introducing biases in the results, all aspects of the analysis, including the

selection, phase space regions, and procedure used to determine the statistical significance of the results, were fixed before the data were examined.

The LHCb detector^{29,30} is designed to collect data of b-hadron decays produced from proton-proton collisions at the Large Hadron Collider. It instruments a region around the proton beam axis, covering the polar angles between 10 and 250 mrad, where approximately 24% of the b-hadron decays occur³¹. The detector includes a high-precision tracking system with a dipole magnet, providing measurements of the momentum and decay vertex position of particle decays. Different types of charged particles are distinguished using information from two ring-imaging Cherenkov detectors, a calorimeter and a muon system. Simulated samples of Λ_h^0 signal modes and control samples are used in this analysis to verify the experimental method and to study certain systematic effects. These simulated events model the experimental conditions in detail, including the proton-proton collision, the decays of the particles, and the response of the detector. The software used is described in refs 32-38. The online event selection is performed by a trigger system that takes fast decisions about which events to record. It consists of a hardware stage, based on information from the

392

NATURE PHYSICS | VOL 13 | APRIL 2017 | www.nature.com/naturephysics

© 2017 Macmillan Publishers Limited, part of Springer Nature. All rights reserved.

ed an

Table 1 Definition of binning scheme A for the decay mode $\Lambda_h^0 \to p\pi^-\pi^+\pi^-$.

Phase space bin	$m(p\pi^+)$	$m(p\pi_{slow}^{-})$	$m(\pi^+\pi^{\text{slow}}), m(\pi^+\pi^{\text{fast}})$	Ф
- Hase space - M	(1.07, 1.23)	9.0		$(0, \frac{\pi}{2})$
	(1.07, 1.23)		a contract of the contract of	$(\frac{\pi}{2},\pi)$
2				$(0, \frac{\pi}{2})$
3	(1.23, 1.35)			$(\frac{\pi}{2},\pi)$
4	(1.23, 1.35)		(+-) .079	$(0, \frac{\pi}{2})$
	(1.35, 5.34)	(1.07, 2.00)	$m(\pi^+\pi^{slow}) < 0.78 \text{ or } m(\pi^+\pi^{fast}) < 0.78$	4
	(1.35, 5.34)	(1.07, 2.00)	$m(\pi^{+}\pi_{slow}^{-}) < 0.78 \text{ or } m(\pi^{+}\pi_{fast}^{-}) < 0.78$	$(\frac{\pi}{2},\pi)$
7	(1.35, 5.34)	(1.07, 2.00)	$m(\pi^{+}\pi_{slow}^{-}) > 0.78$ and $m(\pi^{+}\pi_{fast}^{-}) > 0.78$	$(0, \frac{\pi}{2})$
	(1.35, 5.34)	(1.07, 2.00)	$m(\pi^{+}\pi^{-}_{slow}) > 0.78$ and $m(\pi^{+}\pi^{-}_{fast}) > 0.78$	$(\frac{\pi}{2},\pi$
3	*****	(2.00, 4.00)	$m(\pi^{+}\pi_{\text{slow}}^{-}) < 0.78 \text{ or } m(\pi^{+}\pi_{\text{fast}}^{-}) < 0.78$	$(0, \frac{\pi}{2})$
9	(1.35, 5.34)		$m(\pi^{+}\pi_{slow}^{-}) < 0.78 \text{ or } m(\pi^{+}\pi_{fast}^{-}) < 0.78$	$(\frac{\pi}{2}, \pi$
10	(1.35, 5.34)	(2.00, 4.00)	$m(\pi^{-1}\pi_{slow}) < 0.78$ of $m(\pi^{-1}\pi_{sast}) < 0.78$	$(0, \frac{\pi}{2})$
11	(1.35, 5.34)	(2.00, 4.00)	$m(\pi^+\pi^{slow}) > 0.78$ and $m(\pi^+\pi^{fast}) > 0.78$	4
12	(1.35, 5.34)	(2.00, 4.00)	$m(\pi^{+}\pi_{\text{slow}}^{-}) > 0.78$ and $m(\pi^{+}\pi_{\text{fast}}^{-}) > 0.78$	$(\frac{\pi}{2},\pi$

Binning scheme A is defined to exploit interference patterns arising from the resonant structure of the decay. Bins 1-4 focus on the region dominated by the $\Delta (1232)^{++} \rightarrow p\pi^+$ resonance. The other eight bins are defined to study regions where $p\pi^-$ resonances are present (5-8) on either side of the $\rho(770)^0 \rightarrow \pi^+\pi^-$ resonances (5-12). Further splitting for $|\Phi|$ lower or greater than $\pi/2$ is done to reduce potential dilution of asymmetries, as suggested in ref. 19. Masses are in units of ${\rm GeV}/c^2$

calorimeter and muon systems, followed by a software stage, which applies a full event reconstruction. The software trigger requires Λ_b^0 candidates to be consistent with a b-hadron decay topology, with tracks originating from a secondary vertex detached from the primary pp collision point. The mean Λ_b^0 lifetime is 1.5 ps (ref. 39), which corresponds to a typical flight distance of a few millimetres in the LHCb.

The $\Lambda_h^0 \rightarrow p\pi^- h^+ h^-$ candidates are formed by combining tracks identified as protons, pions, or kaons that originate from a common vertex. The proton or antiproton identifies the candidate as a Λ_b^0 or $\overline{\Lambda}_b^0$. There are backgrounds from b-hadron decays to charm hadrons that are suppressed by reconstructing the appropriate two- or three-body invariant masses, and requiring them to differ from the known charm hadron masses by at least three times the experimental resolution. For the $\Lambda_b^0 \to \Lambda_c^+ \pi^-$ control mode, only the $\Lambda_b^0 \to ph^+h^-\pi^-$ events with reconstructed ph^+h^- invariant mass between 2.23 and 2.31 GeV/c^2 are retained.

A boosted decision tree (BDT) classifier40 is constructed from a set of kinematic variables that discriminate between signal and background. The signal and background training samples used for the BDT are derived from the $\Lambda_b^0 \to pK^-\pi^+\pi^-$ control sample, since its kinematics and topology are similar to the decays under study; background in this sample is subtracted with the sPlot technique⁴¹, a statistical technique to disentangle signal and background contributions. The background training sample consists of candidates that lie far from the signal mass peak, between 5.85 and 6.40 GeV/ c^2 . The control modes $\Lambda_b^0 \to \Lambda_c^+(p\pi^+\pi^-)\pi^-$ and $\Lambda_b^0 \to \Lambda_c^+(pK^-K^+)\pi^-$ are used to optimize the particle identification criteria for the signal mode with the same final state. For events in which multiple candidates pass all selection criteria for a given mode, one candidate is retained at random and the rest discarded.

Unbinned extended maximum likelihood fits to the $p\pi^-\pi^+\pi^$ and the $p\pi^-K^+K^-$ invariant mass distributions are shown in Fig. 2. The invariant mass distribution of the Λ_b^0 signal is modelled by a Gaussian core with power-law tails⁴², with the mean and the width of the Gaussian determined from the fit to data. The combinatorial background is modelled by an exponential distribution with the rate parameter extracted from data. All other parameters of the fit model are taken from simulations except the yields. Partially reconstructed Λ_b^0 decays are described by an empirical function⁴³ convolved with a Gaussian function to account for resolution effects. The shapes of backgrounds from other b-hadron decays due to incorrectly identified particles, for example, kaons identified as pions or protons identified as kaons, are modelled using simulated events. These

consist mainly of $\Lambda_b^0 \to pK^-\pi^+\pi^-$ and $B^0 \to K^+\pi^-\pi^-\pi^+$ decays for the $\Lambda_b^0 \to p\pi^-\pi^+\pi^-$ sample and of similar final states for the $\Lambda_b^0 \to p\pi^-K^+K^-$ sample, as shown in Fig. 2. The yields of these contributions are obtained from fits to data reconstructed under the appropriate mass hypotheses for the final-state particles. The signal yields of $\Lambda_b^0 \to p\pi^-\pi^+\pi^-$ and $\Lambda_b^0 \to p\pi^-K^+K^-$ are 6,646 \pm 105 and $1,030 \pm 56$, respectively. This is the first observation of these decay modes.

Signal candidates are split into four categories according to Λ_b^0 or $\overline{\Lambda}_b^0$ flavour and the sign of $C_{\widehat{\tau}}$ or $\overline{C}_{\widehat{\tau}}$ to calculate the asymmetries defined in equations (1) and (2). The reconstruction efficiency for signal candidates with $C_{\widehat{\tau}} > 0$ is identical to that with C_{7} < 0 within the statistical uncertainties of the control sample, and likewise for $\overline{C}_{\widehat{I}}$, which indicates that the detector and the reconstruction program do not bias this measurement. This check is performed both on the $\Lambda_b^0 \to \Lambda_c^+(pK^-\pi^+)\pi^-$ data control sample and on large samples of simulated events, using yields about 30 times those found in data, which are generated with no CP asymmetry. The CP asymmetry measured in the control sample is $a_{CP}^{7\text{-odd}}(\Lambda_c^+\pi^-) = (0.15 \pm 0.31)\%$, compatible with *CP* symmetry. The asymmetries $A_{\widehat{T}}$ and $\overline{A}_{\widehat{T}}$ in the signal samples are measured with a simultaneous unbinned maximum likelihood fit to the invariant mass distributions of the different signal categories, and are found to be uncorrelated. Corresponding asymmetries for each of the background components are also measured in the fit; they are found to be consistent with zero, and do not lead to significant systematic uncertainties in the signal asymmetries. The values of $a_{CP}^{\widehat{T}\text{-odd}}$ and $a_p^{\widehat{\tau}\text{-odd}}$ are then calculated from $A_{\widehat{\tau}}$ and $\overline{A}_{\widehat{\tau}}$.

In four-body particle decays, the CP asymmetries may vary over

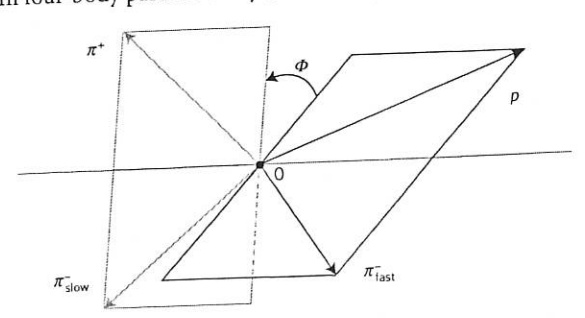
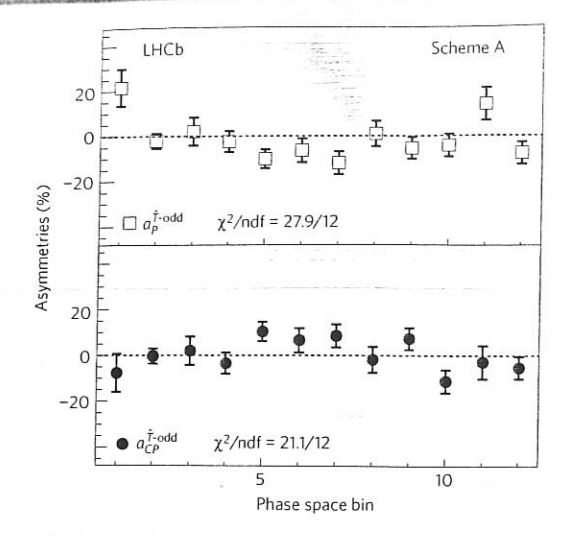


Figure 3 | Definition of the ϕ angle. The decay planes formed by the $p\pi_{\mathsf{fast}}^-$ (blue) and the $\pi_{\rm slow}^-\pi^+$ (red) systems in the Λ_b^0 rest frame. The momenta of the particles, represented by vectors, determine the two decay planes and the angle $\Phi \in [-\pi,\pi]$ (ref. 19) measures their relative orientation.

NATURE PHYSICS | VOL 13 | APRIL 2017 | www.nature.com/naturephysics

al as



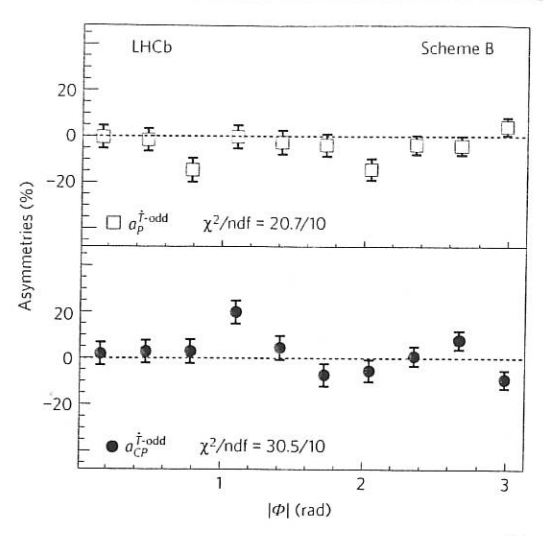


Figure 4 | Distributions of the asymmetries. The results of the fit in each region of binning schemes A and B are shown. The asymmetries $a_P^{\widehat{T}-\text{odd}}$ and $a_{CP}^{T\text{-}\text{odd}}$ for $\Lambda_b^0 \to p\pi^-\pi^+\pi^-$ decays are represented by open boxes and filled circles, respectively. The error bars represent one standard deviation, calculated as the sum in quadrature of the statistical uncertainty resulting from the fit to the invariant mass distribution and the systematic uncertainties estimated as described in the main text. The values of the χ^2 /ndf are quoted for the P- and CP-conserving hypotheses for each binning scheme, where ndf indicates the number of degrees of freedom.

the phase space due to resonant contributions or their interference effects, possibly cancelling when integrated over the whole phase space. Therefore, the asymmetries are measured in different regions of phase space for the $\Lambda_b^0 \to p\pi^-\pi^+\pi^-$ decay using two binning schemes, defined before examining the data. Scheme A, defined in Table 1, is designed to isolate regions of phase space according to their dominant resonant contributions. Scheme B exploits in more detail the interference of contributions which could be visible as a function of the angle Φ between the decay planes formed by the $p\pi_{\text{fast}}^-$ and the $\pi_{\text{slow}}^-\pi^+$ systems, as illustrated in Fig. 3. Scheme B has ten non-overlapping bins of width $\pi/10$ in $|\Phi|$. For every bin in each of the schemes, the Λ_b^0 efficiencies for $C_{\widehat{\tau}} > 0$ and $C_{\widehat{\tau}} < 0$ are compared and found to be equal within uncertainties, and likewise the \overline{A}_b^{ν} efficiencies for $\overline{C}_{\widehat{\tau}}>0$ and $\overline{C}_{\widehat{\tau}}<0$. The analysis technique is validated on the $\Lambda_b^0 \to \Lambda_c^+(pK^-\pi^+)\pi^-$ control sample, for which the angle Φ is defined by the decay planes of the pK^- and $\pi^+\pi^$ pairs, and on simulated signal events.

The asymmetries measured in $\Lambda_b^0 \to p\pi^-\pi^+\pi^-$ decays with these two binning schemes are shown in Fig. 4 and reported in Table 2, together with the integrated measurements. For each scheme individually, the compatibility with the *CP*-symmetry hypothesis is evaluated by means of a χ^2 test, with $\chi^2 = R^T V^{-1} R$, where R is the array of $a_{CP}^{T \text{-odd}}$ measurements and V is the covariance matrix, which is the sum of the statistical and systematic covariance matrices. An average systematic uncertainty, whose evaluation is discussed below, is assigned for all bins. The systematic uncertainties are assumed to be fully correlated; their contribution is small compared to the statistical uncertainties. The p-values of the CPsymmetry hypothesis are 4.9×10^{-2} and 7.1×10^{-4} for schemes A and B, respectively, corresponding to statistical significances of 2.0 and 3.4 Gaussian standard deviations (σ). A similar χ^2 test is performed on $a_p^{\widehat{T} \cdot \text{odd}}$ measurements with p-values for the Psymmetry hypothesis of 5.8×10^{-3} (2.8 σ) and 2.4×10^{-2} (2.3 σ), for scheme A and B, respectively. The overall significance for CPV in $\Lambda_b^0 \to p\pi^-\pi^+\pi^-$ decays from the results of schemes A and B is determined by means of a permutation test⁴⁴, taking into account correlations among the results. A sample of 40,000 pseudoexperiments is generated from the data by assigning each event a random $\Lambda_h^0/\overline{\Lambda}_h^0$ flavour such that *CP* symmetry is enforced. The sign of $C_{\widehat{T}}$ is unchanged if a Λ_b^0 candidate stays Λ_b^0 and reversed if the Λ_b^0 candidate becomes $\overline{\Lambda}_b^0$. The p-value of the CP-symmetry

hypothesis is determined as the fraction of pseudoexperiments with χ² larger than that measured in data. Applying this method to the χ^2 values from schemes A and B individually, the p-values obtained agree with those from the χ^2 test within the uncertainty due to the limited number of pseudoexperiments. To assess a combined significance from the two schemes, the product of the two p-values measured in data is compared with the distribution of the product of the p-values of the two binning schemes from the pseudoexperiments. The fraction of pseudoexperiments whose pvalue product is smaller than that seen in data determines the overall p-value of the combination of the two schemes⁴⁵. An overall p-value of 9.8×10^{-4} (3.3 σ) is obtained for the *CP*-symmetry hypothesis, including systematic uncertainties.

For the $\Lambda_b^0 \to p\pi^- K^+ K^-$ decays, the smaller purity and signal yield of the sample do not permit PV and CPV to be probed with the same precision as for $\Lambda_b^0 \to p\pi^-\pi^+\pi^-$, and therefore only two regions of phase space are considered. One spans $1.43 < m(pK^-) <$ 2.00 GeV/ c^2 (bin 1) and is dominated by excited Λ resonances decaying to pK and the other covers the remaining phase space, $2.00 < m(pK^-) < 4.99 \,\text{GeV}/c^2$ (bin 2). The observables measured in these regions are given in Table 2 and are consistent with CP and P symmetry.

The main sources of systematic uncertainties for both $p\pi^-\pi^+\pi^$ and $p\pi^-K^+K^-$ decays are experimental effects that could introduce biases in the measured asymmetries. This is tested by measuring the asymmetry $a_{CP}^{\hat{7}\text{-odd}}$, integrated over phase space and in various phase space regions, using the control sample $\Lambda_b^0 \to \Lambda_c^+(pK^-\pi^+)\pi^-$, which is expected to exhibit negligible CPV. The results are in agreement with the CP-symmetry hypothesis; an uncertainty of 0.31% is assigned as a systematic uncertainty for the $a_{CP}^{\bar{T}\text{-odd}}$ and $a_p^{\hat{T}\text{-odd}}$ integrated measurements; an uncertainty of 0.60%, the largest asymmetry from a fit to scheme B measurements using a range of efficiency and fit models, is assigned for the corresponding phase space measurements. The systematic uncertainty arising from the experimental resolution in the measurement of the triple products $C_{\widehat{\tau}}$ and $\overline{C}_{\widehat{\tau}}$, which could introduce a migration of events between the bins, is estimated from simulated samples of $\Lambda_h^0 \to p\pi^-\pi^+\pi^-$ and $\Lambda_b^0 \to p\pi^- K^+ K^-$ decays where neither P- nor CP-violating effects are present. The difference between the reconstructed and generated asymmetry is taken as a systematic uncertainty due to this effect, and is less than 0.06% in all cases. To assess the uncertainty associated

NATURE PHYSICS | VOL 13 | APRIL 2017 | www.nature.com/naturephysics

Table 2 | Measurements of CP- and P-violating observables.

	$a_p^{\widehat{T}}$ -odd [%]	$a_{CP}^{\widehat{T}}$ -odd [%]		
Scheme A	$\Lambda_b^0 \to p\pi^-\pi^+\pi^-$			
1 - 1 - 1 - 1 - 1 - 1 - 1 - 1 - 1 - 1 -	21.64±8.28±0.60	$-7.69 \pm 8.28 \pm 0.60$		
2	$-2.04 \pm 3.26 \pm 0.60$	$-0.33 \pm 3.26 \pm 0.60$		
3	$2.03 \pm 6.12 \pm 0.60$	$1.94 \pm 6.12 \pm 0.60$		
4	$-2.45 \pm 4.60 \pm 0.60$	$-3.49 \pm 4.60 \pm 0.60$		
5	$-10.04 \pm 4.13 \pm 0.60$	$10.29 \pm 4.13 \pm 0.60$		
6	$-6.40 \pm 5.23 \pm 0.60$	6.51±5.23±0.60		
7	$-11.91 \pm 5.00 \pm 0.60$	$8.40 \pm 5.00 \pm 0.60$		
8	$0.94 \pm 5.60 \pm 0.60$	$-1.88 \pm 5.60 \pm 0.60$		
9	$-5.38 \pm 4.67 \pm 0.60$	$7.20 \pm 4.67 \pm 0.60$		
10	$-4.26 \pm 4.98 \pm 0.60$	$-11.24 \pm 4.98 \pm 0.60$		
11	$13.94 \pm 7.19 \pm 0.60$	$-2.90 \pm 7.19 \pm 0.60$		
12	$-7.64 \pm 4.79 \pm 0.60$	$-5.35 \pm 4.79 \pm 0.60$		
Scheme B	Section of the Contract of the			
1 1200 121	$-0.42 \pm 4.92 \pm 0.60$	$1.81 \pm 4.92 \pm 0.60$		
2	$-1.63 \pm 4.88 \pm 0.60$	$2.86 \pm 4.88 \pm 0.60$		
3	$-14.73 \pm 5.13 \pm 0.60$	$2.87 \pm 5.13 \pm 0.60$		
4	$-0.32 \pm 4.95 \pm 0.60$	$19.79 \pm 4.95 \pm 0.60$		
5	$-2.71\pm5.16\pm0.60$	$4.47 \pm 5.16 \pm 0.60$		
6	$-3.85 \pm 4.79 \pm 0.60$	$-7.23 \pm 4.79 \pm 0.60$		
7	$-14.40 \pm 4.65 \pm 0.60$	$-5.44 \pm 4.65 \pm 0.60$		
8	$-3.75 \pm 4.14 \pm 0.60$	$0.76 \pm 4.14 \pm 0.60$		
9	$-4.16 \pm 4.01 \pm 0.60$	$7.74 \pm 4.01 \pm 0.60$		
10	$4.21 \pm 3.84 \pm 0.60$	$-9.16 \pm 3.84 \pm 0.60$		
Integrated	$-3.71\pm1.45\pm0.32$	$1.15 \pm 1.45 \pm 0.32$		
Phase space bin	$\Lambda_b^0 \rightarrow p\pi^- K^+ K^-$			
1	3.27 ± 6.07 ± 0.66	$-4.68 \pm 6.07 \pm 0.66$		
2	$4.43 \pm 6.73 \pm 0.66$	$4.73 \pm 6.73 \pm 0.66$		
Integrated	3.62 ± 4.54 ± 0.42	$-0.93 \pm 4.54 \pm 0.42$		
	the second secon			

The CP- and P-violating observables, $a_{Cr}^{T odd}$ and $a_{p}^{T odd}$, resulting from the fit to the data are listed with their statistical and systematic uncertainties. Each value is obtained through an independent fit to a region of the phase space as described in the text and Table 1. Results for schemes A and B are outlined for $\Lambda_b^0 \to p \pi^- \pi^+ \pi^-$ decays, and in two bins of phase space for $\Lambda_b^0 \to \rho \pi^- K^+ K^-$ decays, as defined in the text. The first column lists the bin number. For both decay modes the measurement integrated over the phase space, performed independently, is

with the fit models, alternative functions are used; these tests lead only to small changes in the asymmetries, the largest being 0.05%. For $\Lambda_b^0 \to p\pi^- K^+ K^-$ decays, this contribution is larger, about 0.28% for the $a_{CP}^{\widehat{7}\text{-odd}}$ and $a_p^{\widehat{7}\text{-odd}}$ asymmetries.

Further cross-checks are made to investigate the stability of the results with respect to different periods of recording data, different polarities of the spectrometer magnet, the choice made in the selection of multiple candidates, and the effect of the trigger and selection criteria. Alternative binning schemes are studied as a crosscheck, such as using 8 or 12 bins in $|\Phi|$ for $\Lambda_b^0 \to p\pi^-\pi^+\pi^-$ decays. For these alternative binning schemes, the significance of the CPV measurement of the modified scheme B is reduced to below 3σ . Nonetheless, the overall significance of the combination of these two additional binnings with schemes A and B remains above three standard deviations, with a p-value of 1.8×10^{-3} (3.1 σ), consistent with the 3.3σ result seen in the baseline analysis. An independent analysis of the data based on alternative selection criteria confirmed the results. It used a similar number of events, of which 73.4% are in common with the baseline analysis, and gave p-values for CP symmetry of 3.4×10^{-3} (2.9 σ) for scheme A and 1.4×10^{-4} (3.8 σ) for scheme B.

In conclusion, a search for P and CP violation in $\Lambda_b^0 \to p\pi^-\pi^+\pi^-$ and $\Lambda_b^0 \to p\pi^-K^+K^-$ decays is performed on signal yields of 6,646 \pm 105 and 1,030 \pm 56 events. This is

the first observation of these decay modes. Measurements of asymmetries in the entire phase space do not show any evidence of P or CP violation. Searches for localized P or CP violation are performed by measuring asymmetries in different regions of the phase space. The results are consistent with CP symmetry for $\Lambda^0 \to p\pi^- K^+ K^-$ decays, but evidence for CP violation at the 3.3 σ level is found in $\Lambda_b^0 \to p\pi^-\pi^+\pi^-$ decays. No significant P violation is found. This represents the first evidence of CP violation in the baryon sector, and indicates an asymmetry between baryonic matter and antimatter.

Data availability. All data shown in histograms and plots are publicly available from HEPdata (https://hepdata.net).

Received 16 September 2016; accepted 21 December 2016; published online 30 January 2017

References

- 1. Cabibbo, N. Unitary symmetry and leptonic decays. Phys. Rev. Lett. 10, 531-533 (1963)
- Kobayashi, M. & Maskawa, T. CP violation in the renormalizable theory of weak interaction. Prog. Theor. Phys. 49, 652-657 (1973).
- Sakharov, A. D. Violation of CP invariance, C asymmetry, and baryon asymmetry of the universe. JETP Lett. 5, 24-27 (1967); Sov. Phys. Usp. 34, 392-393 (1991).
- Riotto, A. Theories of Baryogenesis. in In Proc. Summer School in High-energy Physics and Cosmology (eds Gava, E. et al.) 326–436 (World Scientific, 1998). Christenson, J. H., Cronin, J. W., Fitch, V. L. & Turlay, R. Evidence for the 2π
- decay of the K20 Meson. Phys. Rev. Lett. 13, 138-140 (1964).
- Aubert, B. et al. Observation of CP violation in the B0 meson system. Phys. Rev. Lett. 87, 091801 (2001).
- Abe, K. $et\ al.$ Observation of large CP violation in the neutral B meson system. Phys. Rev. Lett. 87, 091802 (2001).
- Aubert, B. et al. Improved measurement of the CKM angle γ in $B^{\mp} \to D^{(*)} K^{(*)\mp}$ decays with a Dalitz plot analysis of D decays to $K_S^0 \pi^+ \pi^-$ and K_s⁰K⁺K⁻. Phys. Rev. D 78, 034023 (2008).
- Poluektov, A. et al. Evidence for direct CP violation in the decay $B^+ \to D^{(*)}K^+$, $D \rightarrow K^{+}\pi^{+}\pi^{-}$ and measurement of the CKM phase ϕ_3 . Phys. Rev. D 81, 112002 (2010).
- 10. Aaij, R. et al. Observation of CP violation in $B^{\pm} \to DK^{\pm}$ decays. Phys. Lett. B 712, 203-212 (2012); erratum 713, 351 (2012).
- 11. Aaij, R. et al. Measurement of CP violation in the phase space of $B^{\pm} \to K^{\pm} \pi^{+} \pi^{-}$ and $B^{\pm} \to K^{\pm} K^{+} K^{-}$ decays. Phys. Rev. Lett. 111, 101801 (2013).
- 12. Aaij, R. et al. First observation of CP violation in the decays of B_s^0 mesons. Phys. Rev. Lett. 110, 221601 (2013).
- Hsiao, Y. K. & Geng, C. Q. Direct CP violation in Λ⁰_b decays. Phys. Rev. D 91, 116007 (2015).
- 14. Bensalem, W. & London, D. T-odd triple-product correlations in hadronic b decays. Phys. Rev. D 64, 116003 (2001).
- 15. Bensalem, W., Datta, A. & London, D. New physics effects on triple-product correlations in Λ_b^0 decays. Phys. Rev. D 66, 094004 (2002).
- 16. Bensalem, W., Datta, A. & London, D. T-violating triple-product correlations in charmless A, decays. Phys. Lett. B 538, 309-320 (2002).
- 17. Sachs, R. G. The Physics of Time Reversal (Univ. Chicago Press, 1987).
- 18. Branco, G. C., Lavoura, L. & Silva, J. P. CP Violation (Oxford Univ. Press, 1999).
- 19. Durieux, G. & Grossman, Y. Probing CP violation systematically in differential distributions. Phys. Rev. D 92, 076013 (2015).
- 20. Durieux, G. CP violation in multibody decays of beauty baryons. JHEP 10, 005 (2016).
- 21. Gasiorowicz, S. Elementary particle physics (Wiley, 1966).
- 22. Bigi, I. I. Y. Charm Physics: Like Botticelli in the Sistine Chapel. Preprint at https://arxiv.org/abs/hep-ph/0107102 (2001).
- 23. Gronau, M. & Rosner, J. L. Triple product asymmetries in K, $D_{(s)}$ and $B_{(s)}$ decays. Phys. Rev. D 84, 096013 (2011).
- 24. Gronau, M. & Rosner, J. L. Triple product asymmmetries in Λ_b^0 and Ξ_b^0 decays. Phys. Lett. B 749, 104-107 (2015).
- 25. Valencia, G. Angular correlations in the decay $B \rightarrow VV$ and CP violation. Phys. Rev. D 39, 3339-3345 (1989).
- 26. Aaij, R. et al. Search for CP violation using T-odd correlations in $D^0 \to K^+ K^- \pi^+ \pi^-$ decays. JHEP 10, 005 (2014).
- 27. Aaij, R. et al. Measurement of b-hadron production fractions in 7 TeV pp collisions. Phys. Rev. D 85, 032008 (2012).

al

- 28. Aaij, R. et al. Study of the kinematic dependences of Λ_h^0 production in pp collisions and a measurement of the $\Lambda_b^0 \to \Lambda_c^+ \pi^-$ branching fraction. JHEP 08, 143 (2014).
- 29. Alves, A. A. Jr et al. The LHCb detector at the LHC. JINST 3, S08005 (2008).
- 30. Aaij, R. et al. LHCb detector performance. Int. J. Mod. Phys. A 30, 1530022 (2015).
- 31. LHCb collaboration. LHC-B: A Dedicated LHC Collider Beauty Experiment for Precision Measurements of CP Violation Letter of intent (CERN-LHCC-95-05, 1995); http://cds.cern.ch/record/290868
- Sjöstrand, T., Mrenna, S. & Skands, P. PYTHIA 6.4 physics and manual. JHEP 05, 026 (2006).
- Sjöstrand, T., Mrenna, S. & Skands, P. A brief introduction to PYTHIA 8.1. Comput. Phys. Commun. 178, 852-867 (2008).
- 34. Belyaev, I. et al. Handling of the generation of primary events in Gauss, the LHCb simulation framework. J. Phys. Conf. Ser. 331, 032047 (2011).
- 35. Lange, D. J. The EvtGen particle decay simulation package. Nucl. Instrum. Meth. A 462, 152-155 (2001).
- 36. Allison, J. et al. Geant4 developments and applications. IEEE Trans. Nucl. Sci. 53, 270-278 (2006).
- 37. Agostinelli, S. et al. Geant4: A simulation toolkit. Nucl. Instrum. Meth. A 506, 250-303 (2003).
- 38. Clemencic, M. et al. The LHCb simulation application, Gauss: design, evolution and experience. J. Phys. Conf. Ser. 331, 032023 (2011).
- 39. Olive, K. A. et al. Review of particle physics. Chin. Phys. C 38, 090001 (2014).
- 40. Breiman, L., Friedman, J. H., Olshen, R. A. & Stone, C. J. Classification and Regression Trees (Wadsworth International Group, 1984).
- 41. Pivk, M. & Le Diberder, F. R. sPlot: a statistical tool to unfold data distributions. Nucl. Instrum. Meth. A 555, 356-369 (2005).
- 42. Skwarnicki, T. A study of the radiative CASCADE transitions between the Upsilon-Prime and Upsilon resonances (Ph.D. thesis, 1986); https://inspirehep.net/record/230779
- 43. Albrecht, H. et al. Search for hadronic $b \rightarrow u$ decays. Phys. Lett. B 241, 278-282 (1990).
- 44. Fisher, R. A. The design of experiments (Oliver and Boyd Ltd., 1935).
- 45. Data analysis in high energy physics (eds Behnke, O., Kröninger, K., Schörner-Sadenius, T. & Schott, G.) (Wiley, 2013).

Acknowledgements

We express our gratitude to our colleagues in the CERN accelerator departments for the excellent performance of the LHC. We thank the technical and administrative staff at the LHCb institutes. We acknowledge support from CERN and from the national agencies: CAPES, CNPq, FAPERJ and FINEP (Brazil); NSFC (China); CNRS/IN2P3 (France); BMBF, DFG and MPG (Germany); INFN (Italy); FOM and NWO (The Netherlands); MNISW and NCN (Poland); MEN/IFA (Romania); MinES and FASO (Russia); MinECo (Spain); SNSF and SER (Switzerland); NASU (Ukraine); STFC (United Kingdom); NSF (USA). We acknowledge the computing resources that are provided by CERN, IN2P3 (France), KIT and DESY (Germany), INFN (Italy), SURF (The Netherlands), PIC (Spain), GridPP (United Kingdom), RRCKI and Yandex LLC (Russia), CSCS (Switzerland), IFIN-HH (Romania), CBPF (Brazil), PL-GRID (Poland) and OSC (USA). We are indebted to the communities behind the multiple open source software packages on which we depend. Individual groups or members have received support from AvH Foundation (Germany), EPLANET, Marie Sklodowska-Curie Actions and ERC (European Union), Conseil Général de Haute-Savoie, Labex ENIGMASS and OCEVU, Région Auvergne (France), RFBR and Yandex LLC (Russia), GVA, XuntaGal and GENCAT (Spain), Herchel Smith Fund, The Royal Society, Royal Commission for the Exhibition of 1851 and the Leverhulme Trust (United Kingdom).

Author contributions

All authors have contributed to the publication, being variously involved in the design and the construction of the detectors, in writing software, calibrating sub-systems, operating the detectors and acquiring data, and finally analysing the processed data.

Additional information

Reprints and permissions information is available online at www.nature.com/reprints. Correspondence and requests for materials should be addressed to N. Neri (nicola,neri@mi.infn.it).

Competing financial interests

The authors declare no competing financial interests.



This article is licensed under a Creative Commons Attribution 4.0 International License, which permits use, sharing, adaptation, distribution and reproduction in any medium or format, as long as

you give appropriate credit to the original author(s) and the source, provide a link to the Creative Commons license, and indicate if changes were made.

The images or other third party material in this article are included in the article's Creative Commons license, unless indicated otherwise in a credit line to the material. If material is not included in the article's Creative Commons license and your intended use is not permitted by statutory regulation or exceeds the permitted use, you will need to obtain permission directly from the copyright holder. To view a copy of this license, visit http://creativecommons.org/licenses/by/4.0/.

NATURE PHYSICS | VOL 13 | APRIL 2017 | www.nature.com/naturephysics

al .

The LHCb collaboration R. Aaij⁴⁰, B. Adeva³⁹, M. Adinolfi⁴⁸, Z. Ajaltouni⁵, S. Akar⁶, J. Albrecht¹⁰, F. Alessio⁴⁰, M. Alexander⁵³, S. Ali⁴³, G. Alkhazov³¹, P. Alvarez Cartelle⁵⁵, A. A. Alves Jr⁵⁹, S. Amato², S. Amerio²³, Y. Amhis⁷, L. An⁴¹, L. Anderlini¹⁸, G. Andreassi⁴¹, M. Andreotti^{17,8}, J. E. Andrews⁶⁰, R. B. Appleby⁵⁶, F. Archilli⁴³, P. d'Argent¹², J. Arnau Romeu⁶, A. Artamonov³⁷, M. Artuso⁶¹, M. Aldreotti, J. E. Allandevs, J. B. Appleoy, J. Alchimi, J. L. Algelit, J. Allandroneu, A. Alchimidov, M. Alcusov, M. Alcusov, M. Baldinolov, M. Baldinolov A. Bay⁴¹, L. Beaucourt⁴, J. Beddow⁵³, F. Bedeschi²⁴, I. Bediaga¹, L. J. Bel⁴³, V. Bellee⁴¹, N. Belloli^{21,i}, K. Belous³⁷, I. Belyaev³², E. Ben-Haim⁸, G. Bencivenni¹⁹, S. Benson⁴³, J. Benton⁴⁸, A. Berezhnoy³³, R. Bernet⁴², A. Bertolin²³, F. Betti¹⁵, M.-O. Bettler⁴⁰, M. van-Beuzekom⁴³, I. Bezshyiko⁴², S. Bifani⁴⁷, P. Billoir⁸, T. Bird⁵⁶, A. Birnkraut¹⁰, A. Bitadze⁵⁶, A. Bizzeti^{18,u}, T. Blake⁵⁰, F. Blanc⁴¹, J. Blouw¹¹, S. Blusk⁶¹, V. Bocci²⁶, T. Boettcher⁵⁸, A. Bondar³⁶, N. Bondar^{31,40}, W. Boniventol⁶, A. Borgheresi^{21,i}, S. Borghi⁵⁶, M. Borisyak³⁵, M. Borsato³⁹, F. Bossu⁷, M. Boubdir⁹, T. J. V. Bowcocck⁵⁴, E. Bowen⁴², C. Bozzi^{17,40}, S. Braun¹², M. Britsch¹², T. Britton⁶¹, J. Brodzicka⁵⁶, E. Buchanan⁴⁸, C. Burr⁵⁶, A. Bursche², J. Buytaert⁴⁰, S. Cadeddu¹⁶, R. Calabrese^{17,8}, M. Calvi^{21,i}, M. Calvo Gomez^{38,m}, A. Camboni³⁸, P. Campana¹⁹, D. Campora Perez⁴⁰, D. H. Campora Perez⁴⁰, L. Capriotti⁵⁶, A. Carbone^{15,e}, G. Carboni^{25,i}, R. Cardinale^{20,h}, A. Cardini¹⁶, P. Carniti^{21,i}, L. Carson⁵², K. Carvalho Akiba², G. Casse⁵⁴, L. Cassillo Garcia⁴¹, M. Cattaneo⁴⁰, Ch. Cauet¹⁰, G. Cavallero²⁰, R. Cenci^{24,i}, M. Charles⁸, Ph. Charpentier⁴⁰, G. Chatzikonstantinidis⁴⁷, M. Chefdeville⁴, S. Chen⁵⁶, S.-F. Cheung⁵⁷, V. Chobanova³⁹, M. Chrzaszcz^{42,27}, X. Cid Vidal³⁹, G. Ciezarek⁴³, P. E. L. Clarke⁵², M. Clemencic⁴⁰, H. V. Cliff⁴⁹, J. Closier⁴⁰, V. Coco⁵⁹, J. Cogan⁶, E. Cogneras⁵, V. Cogoni^{16,40,1}, L. Cojocariu³⁰, G. Collazuol^{23,o}, P. Collins⁴⁰, A. Comerma-Montells¹², A. Contu⁴⁰, A. Cooke⁴⁸, S. Coquereau³⁸, G. Corti⁴⁰, M. Corvo^{17,8}, C. M. Costa Sobral⁵⁰, B. Couturier⁴⁰, G. A. Cowan⁵², D. C. Craik⁵², A. Crocombe⁵⁰, M. Cruz Torres⁶², S. Cunliffe⁵⁵, R. Currie⁵⁵, C. D'Ambrosio⁴⁰, F. Da Cunha Marinho², E. Dall'Occo⁴³, J. Dalseno⁴⁸, P. N. Y. David⁴³, A. Davis⁵⁹, O. De Aguiar Francisco², K. De Bruyn⁶, S. De Capua⁵⁶ Aguiar Francisco², K. De Bruyn⁶, S. De Capua⁵⁶, M. De Cian¹², J. M. De Miranda¹, L. De Paula², M. De Serio^{14,d}, P. De Simone¹⁹, C.-T. Dean⁵³, D. Decamp⁴, M. Deckenhoff¹⁰, L. Del Buono⁸, M. Demmer¹⁰, D. Derkach³⁵, O. Deschamps⁵, F. Dettori⁴⁰, C.-T. Dean³³, D. Decamp⁴, M. Deckenhoff¹⁰, L. Del Buono⁸, M. Demmer¹⁰, D. Derkach³⁵, O. Deschamps⁵, F. Dettori⁴⁰, B. Dey²², A. Di Canto⁴⁰, H. Dijkstra⁴⁰, F. Dordei⁴⁰, M. Dorigo⁴¹, A. Dosil Suárez³⁹, A. Dovbnya⁴⁵, K. Dreimanis⁵⁴, L. Dufour⁴³, G. Dujany⁵⁶, K. Dungs⁴⁰, P. Durante⁴⁰, R. Dzhelyadin³⁷, A. Dziurda⁴⁰, A. Dzyuba³¹, N. Déléage⁴, S. Easo⁵¹, M. Ebert⁵², U. Egede⁵⁵, V. Egorychev³², S. Eidelman³⁶, S. Eisenhardt⁵², U. Eitschberger¹⁰, R. Ekelhof¹⁰, L. Eklund⁵³, Ch. Elsasser⁴², S. Ely⁶¹, S. Esen¹², H. M. Evans⁴⁹, T. Evans⁵⁷, A. Falabella¹⁵, N. Farley⁴⁷, S. Farry⁵⁴, R. Fay⁵⁴, D. Fazzini^{21,i}, D. Ferguson⁵², V. Fernandez Albor³⁹, A. Fernandez Prieto³⁹, F. Ferrari^{15,40}, F. Ferreira Rodrigues¹, M. Ferro-Luzzi⁴⁰, S. Filippov³⁴, R. A. Fini¹⁴, M. Fiorei^{17,8}, M. Fiorini^{17,8}, M. Firlej²⁸, C. Fitzpatrick⁴¹, T. Fiutowski²⁸, F. Fleuret^{7,b}, K. Fohl⁴⁰, M. Fontana^{16,40}, F. Fontanelli^{20,h}, D. C. Forshaw⁶¹, R. Forty⁴⁰, V. Franco Lima⁵⁴, M. Frank⁴⁰, C. Frei⁴⁰, J. Fu^{22,q}, E. Furfaro^{25,i}, C. Färber⁴⁰, A. Gallas Torreira³⁹, D. Galli^{15,e}, S. Gallorini²³, S. Gambetta⁵² M. Gandelman² P. Gandini⁵⁷ V. Gao³ L. M. Garcia Martin⁶⁸ L. Garcia Pardiña a³⁹ D. Galli^{15,e}, S. Gallorini²³, S. Gambetta⁵², M. Gandelman², P. Gandini⁵⁷, Y. Gao³, L. M. Garcia Martin⁶⁸, J. Garcia Pardiñas³⁹, J. Garra Tico⁴⁹, L. Garrido³⁸, P. J. Garsed⁴⁹, D. Gascon³⁸, C. Gaspar⁴⁰, L. Gavardi¹⁰, G. Gazzoni⁵, D. Gerick¹², E. Gersabeck¹², M. Gersabeck⁵⁶, T. Gershon⁵⁰, Ph. Ghez⁴, S. Gianì⁴¹, V. Gibson⁴⁹, O. G. Girard⁴¹, L. Giubega³⁰, K. Gizdov⁵², V. V. Gligorov⁸, D. Golubkov³², A. Golutvin^{55,40}, A. Gomes^{1,a}, I. V. Gorelov³³, C. Gotti^{21,i}, M. Grabalosa Gándara⁵, R. Graciani Diaz³⁸, L. A. Granado Cardoso⁴⁰, E. Graugés³⁸, E. Graverini⁴², G. Graziani¹⁸, A. Grecu³⁰, P. Griffith⁴⁷, L. Grillo^{21,40,i} E. A. Grahado Cardoso -, E. Graverini -, G. Graziani -, A. Grecu--, r. Grimin -, L. Grillo - , S. Grimberg -, C. Graverini -, G. Graziani -, A. Grecu--, r. Grimin -, L. Grillo - , S. R. Gruberg Cazon - , C. Graziani -, A. Grecu--, r. Grimin -, L. Grillo - , G. Hadjivasiliou - , B. R. Gruberg Cazon - , C. Graziani -, A. Grecu--, r. Grimin -, L. Grillo - , C. Hadjivasiliou - , G. Hadjiv S. T. Harnew⁴⁸, J. Harrison⁵⁶, M. Hatch⁴⁰, J. He⁶³, T. Head⁴¹, A. Heister⁹, K. Hennessy⁵⁴, P. Henrard⁵, L. Henry⁸, J. A. Hernando Morata³⁹, E. van Herwijnen⁴⁰, M. Heß⁶⁶, A. Hicheur², D. Hill⁵⁷, C. Hombach⁵⁶, H. Hopchev⁴¹, W. Hulsbergen⁴³, T. Humair⁵⁵, M. Hushchyn³⁵, N. Hussain⁵⁷, D. Hutchcroft⁵⁴, M. Idzik²⁸, P. Ilten⁵⁸, R. Jacobsson⁴⁰, A. Jaeger¹², J. Jalocha⁵⁷, E. Jans⁴³, A. Jawahery⁶⁰, F. Jiang³, M. John⁵⁷, D. Johnson⁴⁰, C. R. Jones⁴⁹, C. Joram⁴⁰, B. Jost⁴⁰, N. Jurik⁶¹, S. Kandybei⁴⁵, W. Kanso⁶, M. Karacson⁴⁰, J. M. Kariuki⁴⁸, S. Karodia⁵³, M. Kecke¹², M. Kelsey⁶¹, I. R. Kenyon⁴⁷, M. Kenzie⁴⁹, T. Ketel⁴⁴, E. Khairullin³⁵, B. Khanji^{21,40,i}, C. Khurewathanakul⁴¹, T. Kirn⁹, S. Klaver⁵⁶, K. Klimaszewski²⁹, S. Koliiev⁴⁶, M. Kolpin¹², I. Komarov⁴¹, R. F. Koopman⁴⁴, P. Koppenburg⁴³, A. Kozachuk³³, M. Kozeiha⁵, L. Kravchuk³⁴, K. Kreplin¹², M. Kreps⁵⁰, P. Krokovny³⁶, F. Kruse¹⁰, W. Krzemien²⁹, W. Kucewicz^{27,i}, M. Kucharczyk²⁷, V. Kudryavtsev³⁶, A. K. Kuonen⁴¹, K. Kurek²⁹, T. Kvaratskheliya^{32,40}, D. Lacarrere⁴⁰, G. Lafferty⁵⁶, A. Lai¹⁶, D. Lambert⁵², G. Lanfranchi¹⁹, C. Langenbruch⁹, T. Latham⁵⁰, C. Lazzeroni⁴⁷, R. Le Gac⁶. J. van Leerdam⁴³. J.-P. Lees⁴, A. Leflat^{33,40}, J. Lefrançois⁷, R. Lefèvre⁵, F. Lemaitre⁴⁰, E. Lemos Cid³⁹, C. Lazzeroni⁴⁷, R. Le Gac⁶, J. van Leerdam⁴³, J.-P. Lees⁴, A. Leflat^{33,40}, J. Lefrançois⁷, R. Lefèvre⁵, F. Lemaitre⁴⁰, E. Lemos Cid³⁹, O. Leroy⁶, T. Lesiak²⁷, B. Leverington¹², Y. Li⁷, T. Likhomanenko^{35,67}, R. Lindner⁴⁰, C. Linn⁴⁰, F. Lionetto⁴², B. Liu¹⁶, X. Liu³, D. Loh⁵⁰, I. Longstaff⁵³, J. H. Lopes², D. Lucchesi^{23,0}, M. Lucio Martinez³⁹, H. Luo⁵², A. Lupato²³, E. Luppi^{17,8}, O. Lupton⁵⁷, A. Lusiani²⁴, X. Lyu⁶³, F. Machefert⁷, F. Maciuc³⁰, O. Maev³¹, K. Maguire⁵⁶, S. Malde⁵⁷, A. Malinin⁶⁷, T. Maltsev³⁶, G. Manca⁷, G. Mancinelli⁶, P. Manning⁶¹, J. Maratas^{5,0}, J. F. Marchand⁴, U. Marconi¹⁵, C. Marin Benito³⁸, P. Marino^{24,t}, J. Marks¹², G. Martellotti²⁶, M. Martin⁶, M. Martinelli⁴¹, D. Martinez Santos³⁹, F. Martinez Vidal⁶⁸, D. Martins Tostes², L. M. Massacrier⁷, A. Massafferri¹, R. Matev⁴⁰, A. Mathad⁵⁰, Z. Mathe⁴⁰, C. Matteuzzi²¹, A. Mauri⁴², B. Maurin⁴¹, A. Mazurov⁴⁷, M. McCann⁵⁵, J. McCarthy⁴⁷, A. McNab⁵⁶, R. McNulty¹³, B. Meadows⁵⁹, F. Meier¹⁰, M. Meissner¹², D. Melnychuk²⁹, M. Merk⁴³, A. Merli^{22,q}, J. McCarthy⁴⁷, A. McNab⁵⁶, R. McNulty¹³, B. Meadows⁵⁹, F. Meier¹⁰, M. Meissner¹², D. Melnychuk²⁹, M. Merk⁴³, A. Merli^{22,q}, J. McCarthy⁴⁷, A. McNab⁵⁶, R. McNulty¹³, B. Meadows⁵⁹, F. Meier¹⁰, M. Meissner¹², D. Melnychuk²⁹, M. Merk⁴³, A. Merli^{22,q}, J. Melnychuk²⁹, M. Merk⁴³, A. Merli^{22,q}, M. Merli²² J. McCartny T., A. McNulty T., B. Meadows T., F. Meir T., M. Meissner T., D. Meinychuk T., M. Merk T., A. Merit M. Merk T., A. Merit M. Meissner T., D. Meinychuk T., M. Merk T., A. Merit M. Moring M. Molina Rodriguez M. A. Monroy M. Morandin M. Morandin M. Morandin M. Morandin M. Morandin M. Morandin M. Mussini M. Muller M. M. Mussini M. Mussini M. Medham M. Neuham M.

al

m

S. Nieswand⁹, R. Niet¹⁰, N. Nikitin³³, T. Nikodem¹², A. Novoselov²⁷, D. P. O'Hanlon⁵⁰, A. Oblakowska-Mucha²⁸, V. Obraztsoy³⁷, S. Ogilvy¹⁹, R. Oldeman⁴⁹, C. J. G. Onderwater⁶⁹, J. M. Otalora Goicochea², A. Otta⁴⁰, P. Owen⁴², A. Oyanguren⁶⁸, P. R. Paisa⁴¹, A. Palanon¹⁴, F. Palaomba²², M. Palutan¹⁹, J. Pannanan¹⁰, A. Papanestis⁵¹, M. Patepagallo¹⁴, L. L. Pappalardo¹⁷⁸, W. Parker⁶⁰, C. Parkes⁵⁶, G. Passales⁵⁶, M. Petros⁵⁷, M. Petrov⁵⁷, M. Petrov⁵⁷, M. Petrov⁵⁷, M. Petrov⁵⁷, M. Petrov⁵⁸, A. Petrolini²⁰⁰, A. Petrov⁵⁷, M. Petrov⁵⁷, M. Petrov⁵⁷, M. Petrov⁵⁷, M. Petrov⁵⁸, A. Polachota Olloqui³⁸, B. Pietrzyk⁴, M. Pikies³⁷, D. Pinci⁵⁸, A. Pistone⁵⁰, A. Pistone⁵⁰, A. Pistone⁵⁰, A. Pistone⁵⁰, A. Petrov⁵⁷, M. Petrov⁵⁷, M. Petrov⁵⁷, M. Poissales⁵⁸, I. Polkalen⁵⁰, E. Polycango⁵⁸, G. Poslave⁵⁸, A. Petrolini²⁰⁰, A. Petrov⁵⁷, M. Petrov⁵⁷, M. Petrov⁵⁷, M. Poissales⁵⁸, I. Polkalen⁵⁸, D. Polkalen⁵⁸, D. Polkalen⁵⁸, D. Polkalen⁵⁸, D. Pistone⁵⁹, G. Pistone⁵⁹, A. Pistone⁵⁹, A. Pittone⁵⁹, P. Polori⁵⁸, A. Pittone⁵⁹, P. Polori⁵⁸, A. Pittone⁵⁹, P. Polori⁵⁸, A. Pittone⁵⁹, P. Rodrigues⁵⁹, P. Solaches⁵⁹, P. Solaches⁵⁹,

Primary affiliations

Centro Brasileiro de Pesquisas Físicas (CBPF), Rio de Janeiro 22290-180, Brazil. ²Universidade Federal do Rio de Janeiro (UFRJ), Rio de Janeiro 21941-972, Brazil. ³Center for High Energy Physics, Tsinghua University, Beijing 100084, China. ⁴LAPP, Université Savoie Mont-Blanc, CNRS/IN2P3, Annecy-Le-Vieux 74941, France. ⁵Clermont Université, Université Blaise Pascal, CNRS/IN2P3, LPC, Clermont-Ferrand 63177, France. ⁶CPPM, Aix-Marseille Université, CNRS/IN2P3, Marseille 12388, France. ⁷LAL, Université Paris-Sud, CNRS/IN2P3, Orsay 91898, France. ⁸LPNHE, Université Pierre et Marie Curie, Université, Paris Diderot, CNRS/IN2P3, Paris 75252, France. ⁹I. Physikalisches Institut, RWTH Aachen University, Aachen D-52056, Germany. ¹⁰Fakultät Physik, Technische Universität Dortmund, Dortmund D-44221, Germany. ¹¹Max-Planck-Institut für Kernphysik (MPIK), Heidelberg D-69029, Germany. ¹²Physikalisches Institut, Ruprecht-Karls-Universität Heidelberg, Heidelberg D-69120, Germany. ¹³School of Physics, University College Dublin, Dublin 4, Ireland. ¹⁴Sezione INFN di Bangia, Bari I-70126, Italy. ¹⁵Sezione INFN di Bologna, Bologna I-40126, Italy. ¹⁶Sezione INFN di Cagliari, Cagliari I-09042, Italy. ¹⁷Sezione INFN di Ferrara, Ferrara I-44100, Italy. ¹⁸Sezione INFN di Bienopa, Bologna I-40126, Italy. ¹⁹Laboratori Nazionali dell'INFN di Frascati, Frascati I-00044, Italy. ²⁰Sezione INFN di Genova, Genova I-16146, Italy. ²¹Sezione INFN di Milano Bicoccca, Milano I-20133, Italy. ²²Sezione INFN di Padova, Padova I-35131, Italy. ²⁴Sezione INFN di Pisa, Pisa I-56127, Italy. ²⁵Sezione INFN di Roma La Sapienza, Roma I-00185, Italy. ²⁷Henryk Niewodniczanski Institute of Nuclear Physics Polish Academy of Sciences, Kraków PL-30-059, Poland. ²⁹National Center for Nuclear Research (NCBJ), Warsaw PL-00-681, Poland. ³⁰Horia Hulubei National Institute of Physics and Nuclear Engineering, Bucharest-Magurele 76900, Romania, ³¹Petersburg Nuclear Physics Institute (PNPI), Gatchina RU-188350, Russia. ³²I

NATURE PHYSICS | www.nature.com/naturephysics

al

recording to a larger of the

es no Of

Fig. Wills Physics Laboratory, University of Bristol, Bristol BS8 1TL, UK. 49 Cavendish Laboratory, University of Cambridge, Cambridge CB3 OHE, UK. 51 CRU Appleton Laboratory, Didot OX11 OQX, UK. 52 School of Physics, University of Warwick, Coventry CV4 7AL, UK. 51 CRU Appleton Laboratory, Didot OX11 OQX, UK. 52 School of Physics and Astronomy, University of Glasgow, Glasgow G12 8QQ, Sics and Astronomy, University of Edinburgh, Edinburgh EH9 3JZ, UK. 53 School of Physics and Astronomy, University of Edinburgh, Edinburgh EH9 3JZ, UK. 55 Imperial College London, London SW7 2BZ, UK. 56 School of Physics and Astronomy, University of University of Uk. 58 Massachusetts Oxford, Oxford OX1 3RH, UK. 58 Massachusetts UK. 54 Oliver Lodge Laboratory, University of Manchester, Manchester M13 9PL, UK. 57 Department of Physics, University of Oxford, Oxford OX1 3RH, UK. 58 Massachusetts Oxford, UK. 59 University of Cincinnati, Cincinnati, Ohio 45221-0011, USA. 60 University of Manchester, Manchester Oxford, USA. 59 University of Cincinnati, Cincinnati, Ohio 45221-0011, USA. 61 University of Uk. 59 University of Cincinnati, UK. 50 Universidade Católica do Rio de Janeiro Uk. 59 University of Uk. 50 University of Cincinnati, Ok. 61 Universidade Católica do Rio de Janeiro College Park, Maryland 20742, USA. 61 Syracuse University, Syracuse, New York 13244-1130, USA. 62 Pontificia Universidade Católica do Rio de Janeiro College Park, Maryland 20742, USA. 61 Syracuse University, Syracuse, New York 13244-1130, USA. 62 Pontificia Universidade Católica do Rio de Janeiro College Park, Maryland 20742, USA. 61 Syracuse University, Syracuse, New York 13244-1130, USA. 62 Pontificia Universidade Católica do Rio de Janeiro Ca College raix, Ivial yianu 20742, USA. Syracuse University, Syracuse, New York 13244-1150, USA. Strontinicia University de Calcula de No de Janeiro (PUC-Rio), Rio de Janeiro 22451-900, Brazil, associated to 2. 63 University of Chinese Academy of Sciences, Beijing 100049, China, associated to 3. 65 December 100049, China de Calcula China Natural Hairway of Particle Physics Control China Natural Hairway of Physics China Natural Hairway of Physi (PUC-KIO), KIO de Janeiro ZZ451-900, Brazil, associated to 2. ⁵³University of Chinese Academy of Sciences, Beijing 100049, China, associated to 3. ⁶⁴Institute of Particle Physics, Central China Normal University, Wuhan, Hubei 430079, China, associated to 3. ⁶⁵Departamento de Fisica, Universidad Nacional de Colombia, Bogota 21716, Colombia, associated to 8. ⁶⁶Institut für Physik, Universität Rostock, Rostock D-18051, Germany, associated to 12. ⁶⁷National December Control Visional Page 21716, Colombia, Bogota 21716, Colo Nacional de Colombia, Bogota 21/16, Colombia, associated to 8. Vinstitut für Physik, Universität Rostock, Rostock D-18051, Germany, associated to 67 National Research Centre Kurchatov Institute, Moscow 123182, Russia, associated to 32. 68 Instituto de Fisica Corpuscular (IFIC), Universität de Valencia-CSIC, Valencia E-46980, Spain, associated to 38. ⁶⁹ Van Swinderen Institute, University of Groningen, Groningen 9747 AG, The Netherlands,

Secondary armiations**Universidade Federal do Triângulo Mineiro (UFTM), Uberaba-MG, Brazil. **Laboratoire Leprince-Ringuet, Palaiseau, France. **P.N. Lebedev Physical Universidade Federal do Triângulo Mineiro (UFTM), Uberaba-MG, Brazil. **Laboratoire Leprince-Ringuet, Palaiseau, France. **P.N. Lebedev Physical Universidade Federal do Triângulo Mineiro (UFTM), Uberaba-MG, Brazil. **Laboratoire Leprince-Ringuet, Palaiseau, France. **P.N. Lebedev Physical Institute, Russian Academy of Science (LPI RAS), Moscow, Russia. **Universidade Federal do Triângulo Mineiro (UFTM), Uberaba-MG, Brazil. **Laboratoire Leprince-Ringuet, Palaiseau, France. **P.N. Lebedev Physical Institute, Russian Academy of Science (LPI RAS), Moscow, Russia. **Universidade Federal do Triângulo Mineiro (UFTM), Uberaba-MG, Brazil. **Laboratoire Leprince-Ringuet, Palaiseau, France. **P.N. Lebedev Physical Institute, Russian Academy of Science (LPI RAS), Moscow, Russia. **Universidade Federal do Triângulo Mineiro (UFTM), Uberaba-MG, Brazil. **Laboratoire Leprince-Ringuet, Palaiseau, France. **Laboratoire Leprince-Ringuet, Palaiseau, France. **P.N. Lebedev Physical Institute, Russian Academy of Science (LPI RAS), Moscow, Russia. **Laboratoire Leprince-Ringuet, Palaiseau, France. **Laboratoire Leprince-Ringuet, Palaiseau, Palais associated to 43. Institute, Russian Academy of Science (LF) RAS), Moscow, Russia. Funiversità di Dari, Dan 1-70120, Italy. Muniversità di Genova, Genova I-16146, Italy. Minversità di Genova, Genova I-16146, Italy. Minversità di Cagliari, Cagliari I-09042, Italy. Minversità di Popo I a Casiona Daria I Octobri Italy. Minversità di Bono I a Casiona Daria I Octobri Italy. Minversità di Bono I a Casiona Daria I Octobri Italy. Minversità di Bono I a Casiona Daria I Octobri Italy. Minversità di Bono I a Casiona Daria I Octobri Italy. Minversità di Bono I a Casiona Daria I Octobri Italy. Minversità di Bono I a Casiona Daria I Octobri Italy. Minversità di Bono I a Casiona Daria I Octobri Italy. Minversità di Bono I a Casiona Daria I Octobri Italy. Minversità di Bono I a Casiona Daria I Octobri Italy. Minversità di Bono I a Casiona Daria I Octobri Italy. Minversità di Bono I a Casiona Daria I Octobri Italy. Minversità di Bono I a Casiona Daria I Octobri Italy. Minversità di Bono I a Casiona Daria I Octobri Italy. Minversità di Bono I a Casiona Daria I Octobri Italy. Minversità di Bono I a Casiona Daria I Octobri Italy. Minversità di Bono I a Casiona Daria I Octobri I Daria I Daria I Casiona Daria I Octobri I Daria I Daria I Casiona Daria I Octobri I Daria Università di Cagilari, Cagilari I-09042, Italy. Oniversità di Ferrara, Ferrara I-44100, Italy. Università di Genova, Genova I-16146, Italy. Università di Roma I-00185, Italy. AGH - Milano Bicocca, Milano I-20133, Italy. Università di Roma Tor Vergata, Roma I-00133, Italy. Università di Roma La Sapienza, Roma I-00185, Italy. Iniversità di Roma I-00185, Italy. Università di Roma I-00186, Italy. Univ Willano Bicocca, Iviliano I-ZUISS, Italy, 'Universita di Roma Tor Vergata, Roma I-UUISS, Italy, "Universita di Roma La Sapienza, Roma I-UUISS, Italy, "Universita di Roma I-UUISS, Italy, "Unive University of Science and rechnology, racuity of Computer Science, Electronics and Telecommunications, Krakow PL-3U-UDA, Poland, "LIFAELS, La Salle, Università di Padova, Padova I-35131, Italy, PUniversità di Pisa, Università Ramon Llull, Barcelona, Spain, "Hanoi University of Science, Hanoi, Vietnam. **OUniversità di Padova, Padova I-35131, Italy, PUniversità di Pisa, Università della Bartinata Della Della Computer Science, Hanoi, Vietnam. **OUniversità di Padova, Padova I-35131, Italy, PUniversità della Bartinata Della Computer Science, Hanoi, Vietnam. **OUniversità di Padova, Padova I-35131, Italy, Puniversità della Computer Science, Hanoi, Vietnam. **OUniversità di Padova, Padova I-35131, Italy, Puniversità di Pisa, Puniversità della Computer Science, Hanoi, Vietnam. **OUniversità di Padova, Padova I-35131, Italy, Puniversità di Pisa, Puniversità della Computer Science, Hanoi, Vietnam. **Ouniversità di Pisa, Puniversità della Computer Science, Hanoi, Vietnam. **Ouniversità di Pisa, Puniversità della Computer Science, Hanoi, Vietnam. **Ouniversità di Pisa, Puniversità della Computer Science, Hanoi, Vietnam. **Ouniversità della Computer Science, Hanoi, Vietnam. Universitat Ramon Llull, Barcelona, Spain. "Hanoi University of Science, Hanoi, Vietnam. "Università di Padova, Padova 1-35131, Italy. "Università della Basilicata, Potenza, Italy. "Università della Basilicata, Potenza, Italy. "Università degli Studi di Milano, Milano I-20133, Italy. "Università di Urbino, Urbino, Italy. "Università degli Studi di Milano, Milano I-20133, Italy. "Università di Urbino, Urbino, Italy. "Università degli Studi di Milano, Milano I-20133, Italy. "Università di Urbino, Urbino, Italy. "Università degli Studi di Milano, Milano I-20133, Italy." Università di Urbino, Urbino, Italy. "Università degli Studi di Milano, Milano I-20133, Italy. "Università di Urbino, Urbino, Italy. "Università degli Studi di Milano, Milano I-20133, Italy." Università di Urbino, Urbino, Italy. "Università degli Studi di Milano, Milano I-20133, Italy." Università di Urbino, Urbino, Italy. "Università degli Studi di Milano, Milano I-20133, Italy." Università degli Studi di Milano, Milano I-20133, Italy. "Università degli Studi di Milano, Milano I-20133, Italy." Università degli Studi di Milano, Milano I-20133, Italy. "Università degli Studi di Milano, Milano I-20133, Italy." Università degli Studi di Milano, Milano I-20133, Italy. "Università degli Studi di Milano, Milano I-20133, Italy." Università degli Studi di Milano, Milano I-20133, Italy. "Università degli Studi di Milano, Milano I-20133, Italy." Università degli Studi di Milano, Milano I-20133, Italy. "Università degli Studi di Milano, Milano I-20133, Italy." Università degli Studi di Milano, Milano I-20133, Italy. "Università degli Studi di Milano, Milano I-20133, Italy." Università di Urbino, Università degli Studi di Milano, Milano I-20133, Italy. "Università degli Studi di Milano, Milano I-20133, Italy." Università degli Studi di Milano, Milano, Milano I-20133, Italy. "Università degli Studi di Milano, Mi risa I-56127, Italy. Puniversita degli Studi di Milano, Milano I-20133, Italy. Universita di Urbino, Urbino, Italy. Universita della basilicata, Potenza, Italy. Scuola Normale Superiore, Pisa, Italy. Università di Modena e Reggio Emilia, Modena, Italy. Iligan Institute of Technology (IIT), Iligan, Philippines.

NATURE PHYSICS | www.nature.com/naturephysics

al



BLACK HOLE PHYSICS

A loud quasi-periodic oscillation after a star is disrupted by a massive black hole

Dheeraj R. Pasham^{1*}, Ronald A. Remillard¹, P. Chris Fragile², Alessia Franchini³, Nicholas C. Stone⁴, Giuseppe Lodato⁵, Jeroen Homan^{6,7}, Deepto Chakrabarty¹, Frederick K. Baganoff¹, James F. Steiner¹, Eric R. Coughlin⁴, Nishanth R. Pasham⁸

The tidal forces close to massive black holes can rip apart stars that come too close to them. As the resulting stellar debris spirals toward the black hole, the debris heats up and emits x-rays. We report observations of a stable 131-second x-ray quasi-periodic oscillation from the tidal disruption event ASASSN-14li. Assuming the black hole mass indicated by host galaxy scaling relations, these observations imply that the periodicity originates from close to the event horizon and that the black hole is rapidly spinning. Our findings demonstrate that tidal disruption events can generate quasi-periodic oscillations that encode information about the physical properties of their black holes.

lmost all massive galaxies are thought to harbor a massive black hole (MBH) [with a mass of $\geq 10^4$ solar masses (M_{\odot}) at their centers (1), yet most of the MBHs are inactive and do not produce any observable electromagnetic radiation. However, once every ~104 to 105 years, a star is predicted to pass near enough to the black hole (BH) to be disrupted by the BH's gravitational forces (2-4). Such episodes, known as tidal disruption events (TDEs) (5), trigger accretion of the debris onto quiescent BHs and provide a brief period of activity. This creates an opportunity to measure the two properties that characterize BHs: mass and spin. Empirical scaling laws can be used to infer BH masses, for example, by using host galaxy properties (6), but the spins of MBHs have been difficult to constrain. This is because the effects of spin predicted by Einstein's general theory of relativity are negligible except in the immediate vicinity of BHs, typically within a few gravitational radii (7). One gravitational radius is $R_g = GM/c^2$, where G, M, and c are the gravitational constant, the BH mass, and the speed of light, respectively. Measuring BH spins requires observations of radiation from the innermost regions of the accretion flow, where gravity is strong. Theoretical models of TDEs predict that shortly after the disruption. a fraction of the stellar debris settles into a hot inner disk with peak thermal emission in the softx-ray or extreme-ultraviolet (UV) range (8). Iden-

¹Kavli Institute for Astrophysics and Space Research, Massachusetts Institute of Technology, Cambridge, MA 02139, USA. ²Department of Physics and Astronomy, College of Charleston, Charleston, SC 29424, USA. ³Department of Physics and Astronomy, University of Nevada, Las Vegas, NV 89154, USA. ⁴Columbia Astrophysics Laboratory, Columbia University, New York, NY 10027, USA. ⁵Dipartimento di Fisica, Università degli Studi di Milano, Milan 20133, Italy. ⁶Eureka Scientific, Oakland, CA 94602, USA. ⁷SRON, Netherlands Institute for Space Research, 3584 CA Utrecht, Netherlands. ⁸Allyo, Mountain View, CA 94040, USA. *Corresponding author. Email: dheeraj@space.mit.edu

tification of such disk-dominated or x-ray-bright TDEs could be used to determine MBH spins.

The transient event ASASSN-14li (right ascension, 12 hours 48 min 15.23 s; declination, $17^{\circ}46'$ 26.22"; J2000.0 equinox) was detected by the All-Sky Automated Survey for Supernovae (ASASSN) on 22 November 2014 (3). It exhibited most of the properties of previously known TDEs: a spatial position consistent with the host galaxy's center [within 160 pc (3)]; a luminosity declining in time with a power law index of $\frac{5}{3}$ (9), as expected for a TDE (10); and a blue optical spectrum with broad hydrogen and helium emission lines and a constant optical color, unlike that of an ordinary supernova (3). ASASSN-14li also produced x-rays (9) and a radio synchrotron flare (11, 12).

The masses of central MBHs are known to correlate with the properties of their host galaxies (6, 13). The velocity dispersion of stars in the inner bulges of galaxies (σ_{vel}) is correlated with the BH mass (M), and this correlation is commonly referred to as the M- σ_{vel} relation (6, 13). The total stellar mass in the bulge and the optical luminosity of the host galaxy are also known to correlate with the BH mass (13). These empirical relations indicate that the RH in ASASSN-14li has a mass in the range of 105.8 to $10^{7.1}~M_{\odot}$ (3, 12, 14). This range is consistent with the BH mass derived independently from physical modeling of ASASSN-14li's multiwavelength light curves (9). The observed x-ray energy spectrum is blackbody-like (thermal) (9, 15, 16), with peak 0.3- to 1.0-keV luminosity of a few times 10^{43} erg/s (Fig. 1). The inferred size of the thermal x-ray-emitting region (~1012 cm) is only a few gravitational radii (9) and remains roughly constant with time (9, 15). This suggests that x-rays from ASASSN-14li originate from an inner accretion flow close to the BH.

In stellar-mass BHs, a sudden onset of accretion often excites quasi-periodic oscillations (QPOs) in the x-ray flux (17). In instances where

the x-ray emission is dominated by the accretion disk, observed QPO frequencies have been used to measure the BH spins (18, 19). We searched for a stable QPO in the soft-x-ray-band (0.3- to 1.0-keV) observations of ASASSN-14li by combining publicly available data from the X-ray Multi-Mirror Mission (XMM-Newton) and Chandra X-ray Observatory space telescopes. We extracted the average power density spectrum (PDS) from data taken at six epochs during the 450 days after ASASSN-14li's discovery (Fig. 1). The combined x-ray PDS shows a feature at 7.65 ± 0.4 mHz (131 s; coherence, Q = centroid frequency/QPO's width = 16 ± 6), as shown in Fig. 2. The highest bin in the QPO is statistically significant at the 4.8σ level (where σ represents statistical significance expressed in multiples of standard deviation) for a search at all frequencies (trials) below 0.5 Hz (Fig. 2A) under the whitenoise hypothesis (noise variations are independent of the time scale). Although the data are consistent with white noise, by assuming the most extreme red noise allowed by the data (i.e., that noise scales inversely with frequency) we derive a conservative lower limit on the statistical significance (false alarm probability) of the highest QPO bin to be 3.9σ (or 10^{-4}) (20).

The QPO is independently detected in the XMM-Newton and Chandra datasets with significance of ≈4σ and ≥2.6σ, respectively, for a search including all frequencies (trials) below 0.5 Hz (20) (fig. S9). We estimated the QPO's fractional root-mean-squared (rms) amplitude during the last XMM-Newton epoch to be 4 ± 1% (Fig. 1) (20). Because the source was bright and the instrument readout was not fast enough in the first four XMM-Newton observations, the data were piled up (20). Thus, similar measurements could not be made for epochs X1 to X4. The Chandra observation was made roughly 420 days after the discovery, by which time ASASSN-14li's flux had declined by ≈10, reducing the pileup (20). The QPO's fractional rms amplitude in Chandra data was 59 ± 11% (Fig. 3) (20). This suggests that between epochs X5 and C1, separated by ~50 days, the fractional rms amplitude of the QPO increased by at least an order of magnitude. After establishing the QPO at 7.65 mHz, we also constructed an average x-ray (0.3- to 1.0-keV) PDS from observations taken by the Neil Gehrels Swift Observatory. The strongest feature in the average Swift PDS is at 7.0 ± 0.5 mHz, consistent with the QPO detected in the XMM-Newton and Chandra datasets

Plotting the Chandra data in imaging mode shows only a single x-ray point source spatially coincident with the galaxy LEDA 043234 (fig. S5). This demonstrates that the QPO does not originate from a nearby contaminating source. The QPO is detected by three different x-ray detectors, establishing that it is not an instrumental artifact but is associated with ASASSN-14li. Movie S1 shows that the QPO signal improves gradually as more power spectra are averaged, implying that the QPO does not originate from a single epoch observation but is present throughout

Pasham et al., Science 363, 531-534 (2019) 1 February 2019

I a

m

at least the first 450 days of the event. The average Swift PDS from data acquired over 500 days, the Chandra PDS from roughly day 420, and the average XMM-Newton PDS all show QPOs at a consistent frequency throughout the first 450 days of the outburst. This implies that the QPO is stable for 3×10^5 cycles (≈ 450 days/131 s). Whereas the stability and coherence of the QPO are similar to those of the QPOs of stellar-mass BHs in a disk-dominated state, the modulation amplitude of >50% (Fig. 3) is higher [e.g., (21)].

An alternative scenario in which the oscillation might be a neutron star pulsation is unlikely for multiple reasons: the large x-ray, optical-UV, and radio photospheric sizes (3, 15, 16, 22); the high bolometric luminosity (15, 16); and the very soft x-ray spectrum (9, 15). In general, the multiwavelength properties of ASASSN-14li are similar to those of many previously known TDEs and unlike those of any known neutron star outburst (see supplementary text).

Assuming ASASSN-14li's BH mass range implied from standard host galaxy scaling relations,

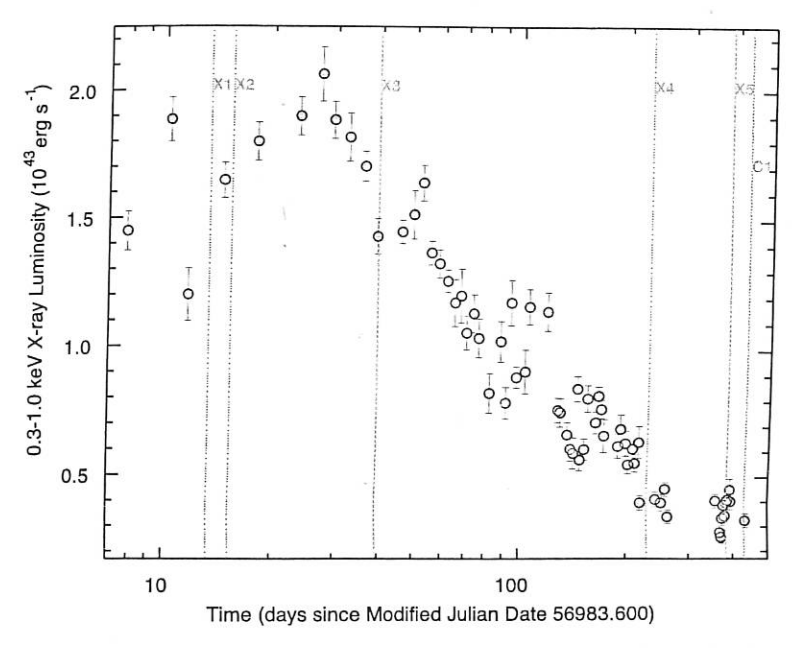
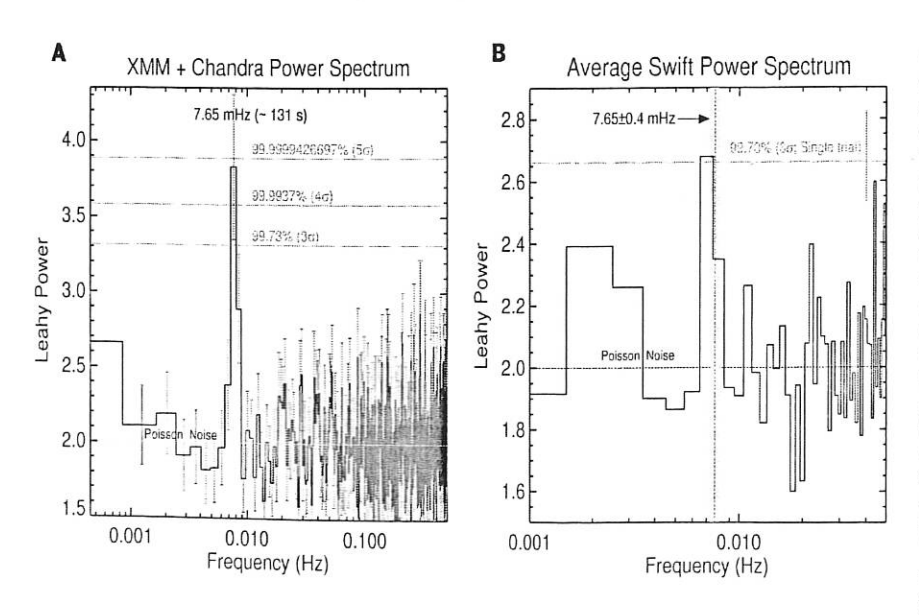


Fig. 1. ASASSN-14Ii's long-term x-ray light curve. The data were taken with Swift [and corrected for pileup (20)]. The dashed vertical lines represent the five epochs of XMM-Newton observations (blue, labeled X1 to X5) and one epoch of Chandra observation (red, labeled C1).



1 February 2019

Pasham et al., Science 363, 531-534 (2019)

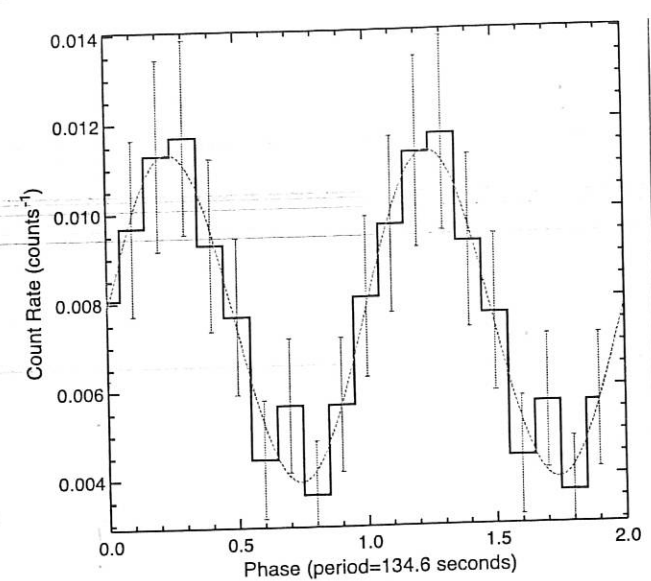
we compared the 7.65-mHz QPO frequency with the five possible frequencies of motion of a test particle orbiting a spinning BH (7, 19). The five frequencies are determined by the BH's mass and spin and the radial distance of the emitting region (supplementary text). In disk-dominated stellar-mass BHs, the inner edges of the accretion disks extend to a constant radius, for a wide range in accretion rates [e.g., (23)]. The natural inner radius predicted by general relativity is the innermost stable circular orbit (ISCO), which depends on BH spin. Because ASASSN-14li appears to be disk dominated, we started our frequency comparison by using the ISCO for the radial distance (Fig. 4). Even at this closest possible location, the only possible solutions are those with a rapidly spinning BH. A lower limit on the BH's dimensionless spin parameter ($a^* = Jc/GM^2$) where J is BH's angular momentum) can be calculated from the BH spin-versus-mass contours shown in Fig. 4. This corresponds to the intersection of the BH mass lower limit and the fastest frequency, which at any given radius is the Keplerian frequency. This implies that ASASSN-14li's spin parameter is greater than 0.7 (Fig. 4). Placing the test particle at any larger radius would only shift this limit to higher spin values. At any given radius, as the other four frequencies (Fig. 4 and supplementary text) are below the Keplerian value, associating the QPO with them would again shift the spin limit to higher values.

If we ignore frequencies higher than the azimuthal (Keplerian) frequency (but see below), then we can interpret Fig. 4 as showing a lower limit on the spin [e.g., (24)] of the MBH that caused the TDE. Alternatively, we can interpret the figure as showing an upper limit of $2\times 10^6 M_{\odot}$ on the BH mass, for a maximum astrophysically plausible spin of $a^*=0.998$ (25). The maximal spin comes from the conjecture that naked singularities (such as BHs with $a^*>1$) are not allowed to exist in nature (26)

Fig. 2. X-ray power spectra for ASASSN-14li, showing a QPO at 7.65 mHz. (A) The average x-ray PDS from eight continuous 10,000-s light curves taken with XMM-Newton and Chandra. The frequency resolution is 0.8 mHz. The strongest feature in the power spectrum lies at a frequency of 7.65 \pm 0.4 mHz (\approx 131 s). The horizontal blue, magenta, and red lines represent the 3, 4, and 5_o white-noise statistical thresholds. The data surrounding the QPO feature are consistent with white noise (20), but we also estimated the QPO significance under red noise. finding that its highest bin is significant at at least the 3.9 revel (20). Uncertainties of ±1 r are shown with gray error bars. Figure S9 shows the XMM-Newton and Chandra data separately. (B) Average Swift PDS from 85 continuous 1000-s light curves with a frequency resolution of 1 mHz. The blue horizontal line shows the 3_o threshold for a single trial search at 7.65 mHz. The highest peak in the power spectrum is at 7.0 ± 0.5 mHz, consistent with the XMM-Newton and Chandra power spectra (fig. S9).

al

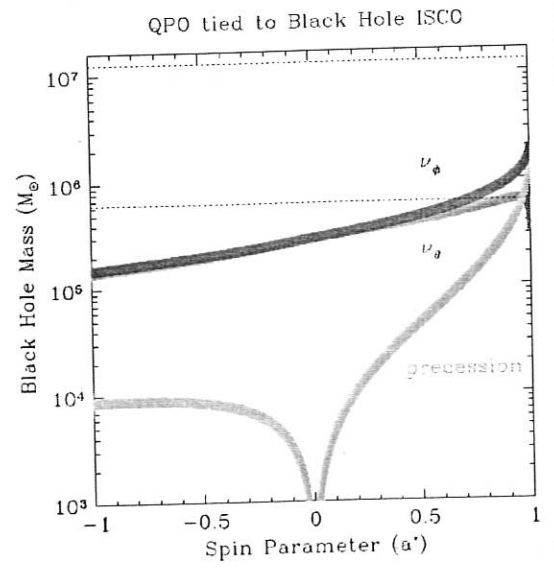
Fig. 3. ASASSN-14li's folded x-ray light curve from Chandra data. The fold period during epoch C1 was estimated by oversampling the light curve (20) to be 134.6 ± 0.1 s (or 7.43 ± 0.006 mHz). The best-fitting sinusoidal curve (dashed line) implies a fractional amplitude of $35 \pm 8\%$, consistent (within the 90% confidence limits) with the estimate from the PDS (fig. S9). The zero phase is arbitrary. and two cycles are shown for clarity. Uncertainties of ±1_o are shown as error bars. Figures S10 and S11 show the folded XMM-Newton



light curves and the evolution of the QPO's rms amplitude, respectively.

Fig. 4. BH dimensionless-spinparameter-versus-mass contours. Spin-versus-mass contours determined by

assuming that the 7.65-mHz QPO is associated with any of three particle frequencies—Keplerian frequency (v_o) (blue), vertical epicyclic frequency (v_θ) (magenta), and Lense-Thirring precession $(v_{\phi} - v_{\theta})$ (green)—at the ISCO, where the radial epicyclic frequency (v_r) is zero and the periastron precession frequency $(v_{\phi} - v_{r})$ is thus equal to the Keplerian frequency (20). The widths of these contours reflect the QPO's width of 0.7 mHz (upper limit). The dashed lines show ASASSN-14li's BH mass range ($10^{5.8}$ to $10^{7.1} M_{\odot}$) estimated from its host galaxy scaling relations. Within this mass range, the only formal



solutions are the ones that require the BH spin parameter to be greater than 0.7.

and the reality that countertorques from radiation absorbed into the BH limit the growth of a* to 0.998 (25).

It is possible that ASASSN-14li's host galaxy and the disrupting BH do not obey the empirical scaling laws (27) and that instead the BH mass is below a value of a few times $10^5 M_{\odot}$. If so, then the BH could have a moderate spin, but this would imply that the BH is an intermediate-mass BH, representing a class of objects whose existence has been controversial [e.g., see (28-30)].

The QPO has a higher dimensionless frequency than those measured from stellar-mass BHs (17): QPO frequency/ $(c^3/GM) > 0.024$, where we have used the lower limit of the estimated BH mass range (14). In stellar-mass BHs, the dimensionless QPO frequencies are ≥0.01 (17). This implies that the radiating material producing the QPO is located close to the BH's event horizon and rules out alternative models for x-ray radiation that require an emitting region far away from the BH. The physical mechanism that produced the QPO remains unclear (supplementary text).

The QPO in ASASSN-14li has further differences from those arising from stellar-mass BHs. The high-frequency QPOs (with frequencies of a few hundred hertz) of accreting stellar-mass BHs

are seen only in hard x-rays (>2 keV) (17) and not in disk-dominated states (21), whereas ASASSN-14li's energy spectrum is very soft (9). The rapid rise in the QPO's rms amplitude is also uncharacteristic of stellar-mass BHs. ASASSN-14li's QPO may represent a different disk oscillation mode from other systems, and thus it may not be valid to compare it directly with known QPOs of stellar-mass BHs.

A quasi-periodicity (at ≈200 s) was previously reported from the TDE SwiftJ164449.3+573451 (SwJ1644+57) (31). However, SwJ1644+57 is an atypical TDE in which the entire electromagnetic radiation was dominated by a jet directly pointing along our line of sight [e.g., (32)]. Radio follow-up indicates that only a small fraction of thermal TDEs launch collimated jets (33), and only a small fraction of such jets would align with our line of sight. SwJ1644+57's periodicity had an amplitude ~1/15 that of ASASSN-14li's and was present only for a short duration of at most a few weeks after its discovery.

High-frequency x-ray QPOs originate from the strong gravity regime in the immediate vicinity of BHs. The stable period of the QPO in ASASSN-14li suggests that it is tied to the physical properties (mass and spin) of the BH at the heart of the disruption.

REFERENCES AND NOTES

- D. Richstone et al., Nature 395, A14-A19 (1998).
- N. C. Stone, B. D. Metzger, Mon. Not. R. Astron. Soc. 455, 859-883 (2016).
- T. W.-S. Holoien et al., Mon. Not. R. Astron. Soc. 455, 2918-2935 (2016).
- S. van Velzen, G. R. Farrar, Astrophys. J. 792, 53 (2014).
- M. J. Rees, Nature 333, 523-528 (1988).
- M. J. Rees, Nature 333, 523-526 (1905).
 K. Gültekin et al., Astrophys. J. 698, 198-221 (2009).
 J. M. Bardeen, W. H. Press, S. A. Teukolsky, Astrophys. J. 178. 347 (1972).
- G. Lodato, E. M. Rossi, Mon. Not. R. Astron. Soc. 410, 359-367 (2011).
- J. M. Miller et al., Nature 526, 542-545 (2015).
- 10. E. S. Phinney, in IAU Symposium, vol. 136, The Center of the Galaxy, M. Morris, Ed. (Springer, 1989), p. 543.
- 11. K. D. Alexander, E. Berger, J. Guillochon, B. A. Zauderer, P. K. G. Williams, Astrophys. J. **819**, L25 (2016). 12. S. van Velzen et al., Science **351**, 62–65 (2016).
- N. J. McConnell, C.-P. Ma, Astrophys. J. 764, 184 (2013).
 T. Wevers et al., Mon. Not. R. Astron. Soc. 471, 1694–1708 (2017).
- 15. J. S. Brown et al., Mon. Not. R. Astron. Soc. 466, 4904–4916 (2017)
- 16. D. R. Pasham et al., Astrophys. J. 837, L30 (2017).
- J. E. McClintock, R. A. Remillard, in Compact Stellar X-ray Sources, W. Lewin, M. van der Klis, Eds. (Cambridge Univ. Press, 2006). pp. 157-213.
- A. Franchini, S. E. Motta, G. Lodato, Mon. Not. R. Astron. Soc. 467, 145-154 (2017).
- S. E. Motta, T. M. Belloni, L. Stella, T. Muñoz-Darias, R. Fender, Mon. Not. R. Astron. Soc. 437, 2554-2565 (2014).
- 20. Materials and methods are available as supplementary materials.
- J. Homan et al., Astrophys. J. 132 (suppl.), 377-402 (2001). 22. D. R. Pasham, S. van Velzen, Astrophys. J. 856, 1 (2018).
- 23. J. F. Steiner et al., Astrophys. J. 718. L117–L121 (2010). 24. T. E. Strohmayer, Astrophys. J. 554, L169–L172 (2001).
- 25. K. S. Thorne, Astrophys. J. 191, 507 (1974).
- 26. R. Penrose, Riv. Nuovo Cimento 1, 252-276 (1969) 27. J. E. Greene et al., Astrophys. J. 721, 26-45 (2010).
- 28. D. R. Pasham, T. E. Strohmayer, R. F. Mushotzky, Nature 513. 74-76 (2014)
- 29. A. W. Graham, N. Scott, Astrophys. J. 798, 54 (2015).
- 30. M. Mezcua, Int. J. Mod. Phys. D 26, 1730021 (2017).

al is

1 February 2019 Pasham et al., Science 363, 531-534 (2019)

Downloaded from http://science.sciencemag.org/ on June 23, 2019

- 31. R. C. Reis et al., Science 337, 949–951 (2012). 32. J. S. Bloom et al., Science 333, 203–206 (2011). 33. A. Generozov et al., Mon. Not. R. Astron. Soc. 464, 2481–2498
- 34. XMM-Newton Science Archive, http://nxsa.esac.esa.int/ nxsa-web/.
- 35. Chandra X-ray Center Data Archive, http://cxc.harvard.edu/ cda/.
- 36. Swift Archive, http://heasarc.nasa.gov/docs/swift/archive/.

ACKNOWLEDGMENTS

D.R.P. thanks D. Huenemoerder, A. Ingram, P. Uttley, and M. Nowak for valuable discussions. This work is based on observations made with the XMM-Newton Chandra, and Swift observatories. Funding: D.R.P., E.R.C., J.F.S., and N.C.S. were supported by NASA through the Einstein Fellowship Program. grants PF6-170156, PF6-170150, PF5-160144, and PF5-160145. respectively. N.C.S. also received financial support from NASA through the Astrophysics Theory Program, grant NNX17AK43G.

F.K.B. received financial support from NASA through SAO F.K.B. received tinancial support from NASA through SAO award SV2-8023, issued by the Chandra X-ray Observatory Center, which is operated by the Smithsonian Astrophysical Observatory for and on behalf of NASA under contract NASS-03060. Author contributions: D.R.P. led the overall project. R.A.R. provided Fig. 2 and contributed to the interpretation of the results. P.C.F. A.F. N.C.S., G.L., J.H., D.C., F.K.B., J.F.S., and E.R.C. contributed toward the theoretical implications of the results. P.C.F., N.C.S., G.L., and A.F. wrote the discussion on physical mechanisms for the QPO, D.C. and R.A.R. assisted with the Monte Carlo simulations to test the statistical significance of the QPO, F.K.B. and D.C. contributed toward ruling out a pulsar origin. N.R.P. assisted with the setup and parallelization of the Monte Carlo simulations. Competing interests: The authors declare that there are no competing interests, Data and materials availability: The x-ray observations are available in the observatory archives: NAS8-03060. Author contributions: D.R.P. led the overall no competing interests. Data and materials availability: The x-ray observations are available in the observatory archives: XMM-Newton (34). Chandra (35). and Swift (36). Observation identifiers for Chandra and XMM-Newton are listed in

table S1: for Swift they range from 00033539001 to 00033539097 inclusive. Our derived unbinned XMM-Newton-Chandra PDS, as plotted in Fig. 2, is provided as data S1. Our code for the red-noise Monte Carlo simulations is supplied in data S2.

SUPPLEMENTARY MATERIALS

www.sciencemag.org/content/363/6426/531/suppl/DC1 Materials and Methods Supplementary Text Figs. S1 to S11 Tables S1 to S4 References (37-85) Movie S1 Data S1 and S2

14 December 2017; accepted 12 December 2018 Published online 9 January 2019 10.1126/science.aar7480

Pasham et al., Science 363, 531-534 (2019) 1 February 2019

4 of 4

Cel

Science

A loud quasi-periodic oscillation after a star is disrupted by a massive black hole

Dheeraj R. Pasham, Ronald A. Remillard, P. Chris Fragile, Alessia Franchini, Nicholas C. Stone, Giuseppe Lodato, Jeroen Homan, Deepto Chakrabarty, Frederick K. Baganoff, James F. Steiner, Eric R. Coughlin and Nishanth R. Pasham

Science 363 (6426), 531-534.

DOI: 10.1126/science.aar7480originally published online January 9, 2019

Oscillating x-rays reveal black hole spin

When a star passes close to a massive black hole (MBH), it is ripped apart by the strong tidal forces. As the resulting debris falls toward the MBH, it heats up, emitting light and x-rays in a tidal disruption event (TDE). Pasham et al. examined x-ray observations of a TDE that occurred in 2014. The x-ray emissions varied in a quasi-periodic oscillation every 131 seconds. The rapid rate of this oscillation could only have arisen from material orbiting close to the MBH's event horizon, which indicates that the MBH's event horizon which indicates the think in the material orbiting t MBH's event horizon, which indicates that the MBH is spinning rapidly. Science, this issue p. 531

ARTICLE TOOLS

http://science.sciencemag.org/content/363/6426/531

SUPPLEMENTARY MATERIALS

http://science.sciencemag.org/content/suppl/2019/01/08/science.aar7480.DC1

REFERENCES

This article cites 73 articles, 4 of which you can access for free http://science.sciencemag.org/content/363/6426/531#BIBL

PERMISSIONS

http://www.sciencemag.org/help/reprints-and-permissions

Use of this article is subject to the Terms of Service